

# Spiroheterocyclic Photocatalyst for Reducing QHIn-Persistent Pollutants, Dyes, and Transition-Metal Ions Cocatalyzed with Electrolytes

Renu Kumari and Man Singh\*

Cite This: *ACS Omega* 2022, 7, 40203–40229

Read Online

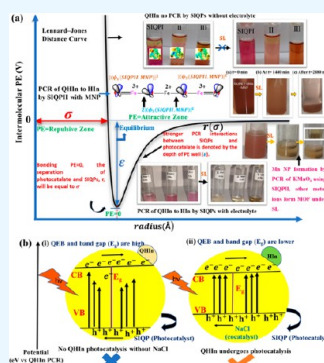
ACCESS |

Metrics &amp; More

Article Recommendations

Supporting Information

**ABSTRACT:** The 7-nitro-2'-phenyl-5',6',7',7a'-tetrahydrospiro[indeno[1,2-*b*]quinoxaline-11,3'-pyrrolizine]-1',1'(2'*H*)-dicarbonitrile (SIQPI), 2'-(4-cyanophenyl)-7-nitro-5',6',7',7a'-tetrahydrospiro[indeno[1,2-*b*]quinoxaline-11,3'-pyrrolizine]-1',1'(2'*H*) dicarbonitrile (SIQPPII), and 2'-(4-methoxyphenyl)-7-nitro-5',6',7',7a'-tetrahydrospiro[indeno[1,2-*b*]quinoxaline-11,3'-pyrrolizine]-1',1'(2'*H*)-dicarbonitrile (SIQPPIII) were used to photocatalyze quinonoid phenolphthalein (QHIn) in aq-ACN-EtOH (mixed solvent) with NaCl and KCl electrolytes. SIQPI, II, and III spiroindenoquinoxaline pyrrolidines (SIQPs) as spiroheterocyclic photocatalysts alone could not reduce QHIn, but with the addition of electrolytes they are reduced via  $\pi$  cationic interactions (PCI). SIQPI, II, and III with NaCl reduced QHIn in 120, 28, and 50 min, unlike in 138, 58, and 63 min with KCl in mixed solvent. SIQPI, II, and III alone have reduced methylene blue (MB) in 120, 45, and 70 min, unlike in 110, 27, and 55 min with graphene oxide (GO), whereas with NaCl and KCl they are reduced in 82, 36, and 44 min and 89, 43, and 50 min, respectively. SIQPs with GO had reduced MB in less time than the SIQPs alone, and SIQPs with NaCl had reduced QHIn in a shorter time than KCl. The electrolytes have cocatalyzed a reduction of dyes under sunlight (SL). The electrolytes have reduced a quinonoid structure (QS) and dyes by generating negative and positive ( $e^-$  and  $h^+$ ) holes in a shorter time. SIQPPII and magnetic nanoparticles (MNPs) of 58 nm with NaCl photocatalyzed the QHIn in 2880 min. The SIQPs also reduced methyl orange (MO) and brilliant blue R (BBR) at variable temperature (*T*) and pH range, whereas SIQPs have developed a molecular organic framework (MOF) with transition-metal salts ( $\text{NiCl}_2$ ,  $\text{CrO}_3$ ,  $\text{KMnO}_4$ ,  $\text{CuSO}_4$ , and  $\text{MnCl}_2$ ) on photocatalysis.



## 1. INTRODUCTION

SIQPs with a higher polarizability have negligible conductivity ( $4 \times 10^{-6} \text{ S cm}^{-1}$ ) (Figures 1 and S1(a–c)). The SIQPs and GO both have photocatalytically reduced (PCR) the MB<sup>1</sup> individually and together. These experiments have inspired us to reduce QHIn, BBR, MO, and transitional-metal ions by SIQPs. SIQPs alone have reduced BBR and MO at pH 4 and 8 and formed a MOF with the transition metals but could not reduce the QHIn at pH 8 in the absence of electrolytes under SL. Phenolphthalein (HIn) with aq-NaOH is transformed into QHIn having an electronically stable QS. Thus, the QS having high potential inhibited the electronic oscillations or excitation to a higher energy state as a harmonized wave function ( $\psi$ ). The electronic harmonization is weakened by electrolytes via developing PCI with the QHIn using short sized  $\text{Na}^+$  unlike  $\text{Ba}^{2+}$  ( $\text{BaCl}_2$ ) for reduction at constant pH and split of water. Also, the electrolytes have cocatalyzed the SIQPs to enhance an intensity of  $\psi$  of the  $e^-$  and  $h^+$  holes where the  $e^-$  and  $h^+$  holes have counterbalanced the respective holes of the reducing species by minimizing their quantum energy barrier (QEB) with a high quantum yield ( $\Phi$ ). The ions of the electrolytes could have aligned the electrostatic sites of the SIQPs with QHIn via enhancing redox cycles (ROC). This route to SIQPs–electrolyte interfaces could lead to a greener<sup>2</sup> PCR mechanism

for QHIn, a persistent pollutant by SIQPs at constant pH. Also, SIQPs with MNPs could not reduce the QHIn but were reduced with electrolyte in 48 h. The MNPs seem to align the QHIn with stronger adhesive forces and have generated high QEB and permittivity ( $\epsilon$ ), and the holes fail to overcome these barriers. The PCR of dyes was analyzed with UV–vis and fluorescence spectroscopy via photochemical and quantum activities of SIQPs, which have not been reported yet (Table S1). Transitional metallic sulfide<sup>3</sup> nanoparticles (NPs) doped with GO have enhanced MB reduction by 18.29%. Similarly, they have resonated the energy of SIQPs to reduce QHIn. The resonating QS transferred their energy to PCR and polarizability supported dipole–dipole resonance energy transfer (DRET) via Forster resonance energy transfer<sup>4</sup> (FRET); e.g., SIQPPII with 2CN and CN via chiral a carbon atom (CCA) could have aligned the dipoles to PCR dyes. The  $\text{Na}^+$  and  $\text{Cl}^-$  align a solvent to reorient and respond to  $e^-$  and  $h^+$  holes. The zeta potential ( $\zeta$ )

Received: August 9, 2022

Accepted: October 13, 2022

Published: October 26, 2022



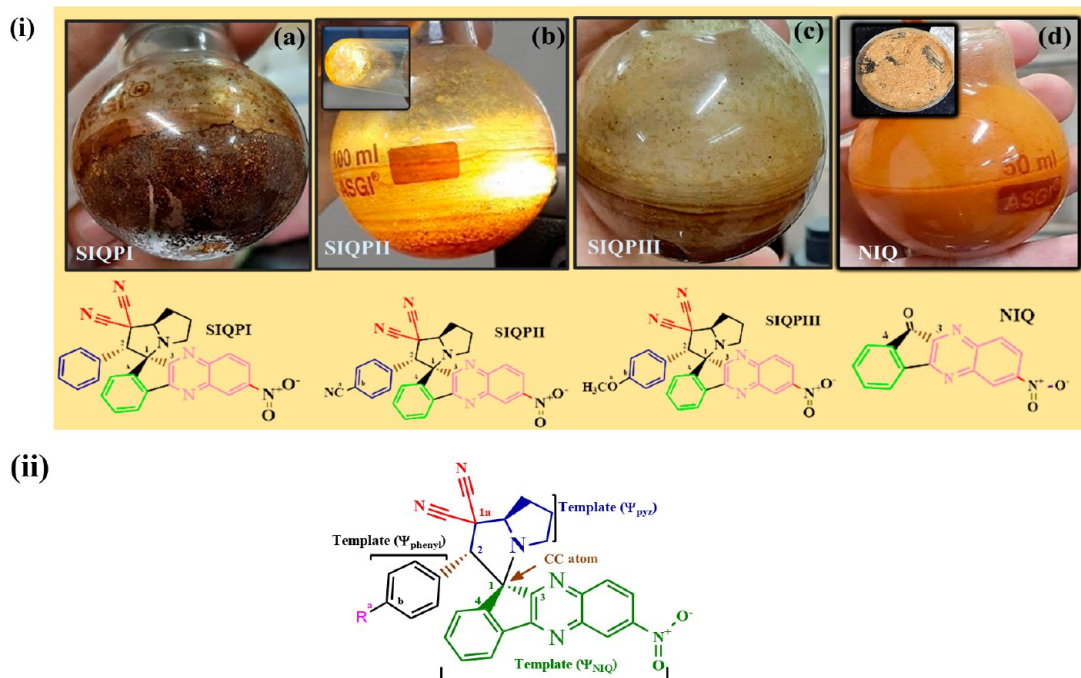


**Figure 1.** (i) SIQP (a) I, (b) II, (c) III, and (d) NIQ appearances and spatial geometrical configurations. (ii) SIQP functional sites and CCA with different templates.

of SIQPs develop a DRET with electron-releasing (ERG) and electron-withdrawing functional groups (EWG). The electrolytes seem to transform a potential energy (PE) to kinetic energy (KE) to photocatalyze the QHIn via disrupting QS and aligning SIQPs for higher polarizability. The CCA induces a polarizability by aligning electronic sites of the SIQPs to reduce dyes. The SIQPs with electrolytes increase a mean free path (MFP) of holes enhanced by minimizing QEB to drastically reduce<sup>5</sup> the QHIn. The electrolytes promote harmonic oscillations to enhance polarizability of SIQPs<sup>6,7</sup> to PCR the QHIn. Despite large advancements in photocatalysts, their simulation with electrolyte was never explored. Also, the electrolytes have mutually solubilized a diphasic medium to monodisperse the SIQPs for a quick photon ( $h\nu$ ) response to PCR a dye as there is no single solvent that can homogenize both the photocatalyst and cocatalyst. The different electronic configurations of SIQPs align with the electrolytes to disrupt QS for PCR. The persistent pollutants harm a whole environment but no photocatalysts are there to dissolve and photodegrade them. The SIQPs in mixed solvent with electrolytes on widening the solubilizing activities have reduced QHIn contrary to MNPs<sup>8</sup> (Table 1).

## 2. RESULTS AND DISCUSSION

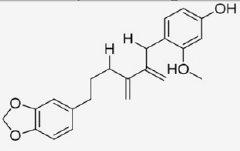
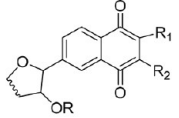
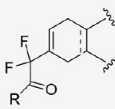
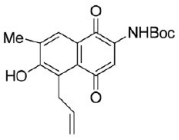
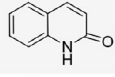
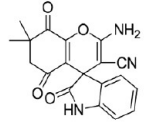
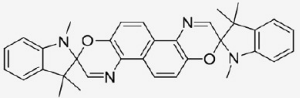
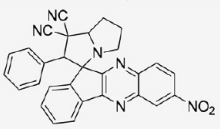
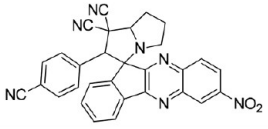
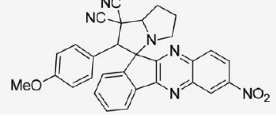
CCA connects nitroindenoquinoxaline-11-one (NIQ) ( $\psi_{NIQ}$ ), the phenyl ring, and pyrrolidine (pyz) ( $\psi_{pyz}$ ) of the SIQPs template as  $\psi_{NIQ} > CCA < \psi_{pyz}$  that selectively responds to  $h\nu$  (Figure 1). The CCA aligns oscillations of SIQPs with certain  $\psi$  in a symmetric wavevector enhancing the electronic probability<sup>1</sup>  $|\psi|^2$ . Free phenyl (FP) of SIQPI aligns the  $e^-$  and  $h^+$  holes whereas the NC-phenyl of II and H<sub>3</sub>CO-phenyl with III reorient the electronic clouds via spatial  $\psi_{NIQ}$  and  $\psi_{pyz}$  notches. The SIQPs reduced MB in aq-ACN<sup>1</sup> and extended to photocatalyze the QHIn, BBR, MO, and transition-metal ions in the presence of electrolytes in mixed solvent. The SIQPs alone failed to PCR the QHIn due to its QS with a higher QEB. The QS disruption has been challenged due to highly aligned electronic configurations

with a minimum energy of 53.87 kcal/mol and dipole–dipole of 5.12 D than HIn with 22.89 kcal/mol and 8.29 D inhibiting the H bonding. The QS restricts HOMO  $\rightarrow$  LUMO via  $\pi \rightarrow \pi^*$  with symmetric  $\psi$  to maintain an electronically equilibrated structure with no stretching frequency difference ( $\Delta\nu = 0$ ). The  $\Delta\nu = 0$  state could not generate a spontaneity with QHIn unlike other dyes with electron-deficient sites to attract the  $e^-$  and  $h^+$  holes. Therefore, the Na<sup>+</sup> and Cl<sup>-</sup> interact with QHIn as the electrons of its double bonds develop electronic spins with a higher oscillating energy to intensify the  $\psi$  with a large number of  $e^-$  and  $h^+$  holes. The  $\psi_{SIQPs}$  with dipole resonance connects the  $\psi_{QHIn}$  mutually via DRET.

**2.1. DLS Analysis.** The holes align and generate the polarizability, PDI,  $\zeta$ , surface charges, and particle% passage (Figures 2 and S2). Fractional positive and negative charges of NIQ and pyz respond to  $h\nu$  to align the charges and develop the  $\zeta$  with higher photocatalytic activities. The linkages of a solvent align the  $e^-$  and  $h^+$  holes around CCA by averting intermixing of  $\psi$  electronic clouds of pyz and NIQ individually to avoid their recombination. The CCA avoids collisions of holes for a longer MFP to contact the  $\psi_{QHIn}$ . The electronically rich and deficient holes oscillate with  $\psi_-$  and  $\psi_+$  to interact with the respective sites of QHIn and the other dyes to hybridize with  $|\psi|^2$ . The  $\psi_{solvent}$  with a moderately reversible interaction get activated to align with active charges of the dyes. The sharp distribution of SIQPI infers fewer interacting sites with solvent than SIQP II and III. The NC-phenyl EWG and H<sub>3</sub>CO-phenyl ERG ( $e^-$  and  $h^+$ ) disrupt a delocalization to generate another center with certain hole density. SIQP II and III are not sharply distributed size wise and generate different  $\zeta$  compared to I due to FP (Figure 2). SIQPs realign holes with a higher  $\zeta$  to enhance a photocatalytic reduction of QHIn as their electronic sites oscillate with certain  $\psi$ . The  $\psi$  of the  $e^-$  and  $h^+$  holes of SIQPs interact with  $\psi_{solvent} e^-$  and  $\psi_{solvent} h^+$  to align with prominent charges of dyes.

**2.2. XRD Analysis.** NIQ, pyz, and FP lattices around CCA have generated electronic intensities contrary to CN/EWG that

Table 1. Comparative PCR for Heterocyclic Compounds with SIQPs for Dye

Sr. No.	Heterocyclic Compounds	QHIn PCR
1.		Not reported
2		Not reported
3		Not reported
4		Not reported
5		Not reported
6		Not reported
7		Not reported
<b>Spiroheterocyclic compounds PCR QHIn with NaCl (cocatalyst)</b>		
8		$\Phi = 76.7\%$
9		$\Phi = 75.6\%$
10		$\Phi = 72\%$

did not develop independent peaks except for CCA (Figure 3). The SIQPII filters  $\psi$  compared to  $I$  with delocalized electron cloud center in continuity of CCA. The SIQPI having FP and connected to pyz via CCA and NIQ with different  $\pi$  conjugated systems split sharply. The intensified delocalized FP with multiple sharper peaks is unable to conjugate with other units. NIQ peaks with different intensities and vibrations due to a residual  $e^-$  charge along the lattices, differing from SIQPI by FP so the CCA mildly tunes the FP, NIQ, and pyz. The SIQPI attains a crystalline structure with  $\alpha$  (NIQ) and  $\beta$  (phenyl and pyz) templates. NIQ, pyz, and FP, the negatively charged delocalized centers, sharpened the peaks at the  $>2\theta$  value

(Figure 3). Their electronic clouds with dipole–dipole interaction (DDI) transfer mutually around the CCA. The CCA equilibrates their surface charges with different electronic clouds to influence the electronic scintillations. XRD<sup>9</sup> has predicted the overall charges, size, and lattice alignments at certain  $d$  spacing vis-à-vis inner orbital electrons; e.g., FP of SIQPI induces a milder photocatalytic activity with a weaker coordination among the pyz and NIQ. These may not minimize a QEB unlike the II and III with EWG and ERG, respectively. Had there been a closely packed template structure then there would have not been a chance to respond to the  $h\nu$  similar to the QS. Their symmetric oscillations configure a single sharper



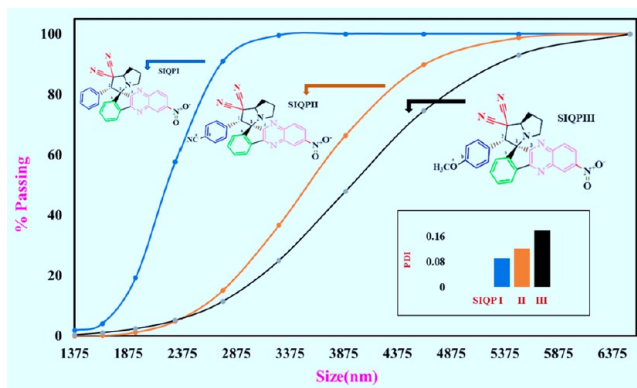


**Figure 2.** Size and PDI of SIQPI, II, and III vis-à-vis delocalization of FP, EWG, and ERG, respectively.

lattice. The CCA coordinated the NIQ, pyz, and FP but could not produce their own lattices (Figure 3). The CCA with CN equilibrates the  $\psi_{\text{NIQ}}$  and  $\psi_{\text{pyz}}$  as no sharper peaks exist except as hedges generating a spontaneity due to their peripheral positions. Thus, a SIQPII acts as a single unit around CCA with no intense peak except ROC to photocatalyze MB in a shorter time (Figure 3). Had there been no charges then the SIQPII could have not photocatalyzed<sup>10</sup> the QHIn without electrolyte, but it reduced in 28 min with electrolyte. The reduction in time with electrolyte infers the holes generate activities of SIQPs due to the ionic interactions. The electrolytes have disrupted QS of the QHIn to minimize a QEB. Unlike MB, no electron-rich or -deficient sites exist with QHIn, so its oscillations generate a weaker  $\psi$  to minimize with a high QEB. The SIQPII with NC-phenyl/EWG has induced a DRET. The CCA synchronizes NIQ, NC-phenyl, or pyz by equilibrating their oscillations as CN aligns delocalization linearly. XRD peaks with a higher intensity split at  $2\theta = 25^\circ$  as the CN SIQPII are unable to align the lattices as they could not cross over the SIQP of CCA (Figure 3). The electronic clouds of SIQPII with multiple splits could robustly counterbalance the  $\psi$  of QHIn compared to I. The CCA orients the NC-phenyl, 2NC-pyz, and NIQ in 3D to intensify the ROC. SIQPI<sup>11</sup> has sharpened the peaks unlike aligned  $h^+$  and  $e^-$  hole generation with a weaker photocatalysis. The FP and ERG have developed sharper peaks compared to EWG with closely placed peaks (Figure 3). With CN, the peaks are neither fully aborted nor developed due to an electronic distribution of different functional sites. The reoriented electronic clouds of EWG and ERG act as an acoustic sensor. Intensity patterns of peaks with a hydrophobic OCH<sub>3</sub> differ from II with hydrophilic<sup>12,13</sup> CN. The CN of

SIQPII vis-à-vis 2CN/EWG of pyz intensified the peak at  $2\theta = 27^\circ$ . Each CN electronically interconnected has caused electron–electron repulsion (EER) oscillations centered around CCA (Figure 3). The OCH<sub>3</sub> compared to CN of II has produced sharper peaks due to a direction of electron clouds from OCH<sub>3</sub> to template and from template to CN around CCA, respectively. The NO<sub>2</sub>/EWG of NIQ developed the sharper lattice peaks while the OCH<sub>3</sub>/ERG of phenyl could continue oscillations with EWG. The phenyl could orient the SIQPs lattice if it is bonded with ionic liquid,<sup>14</sup> metallic NPs, DNA, proteins, and others. These systems could develop the advanced biocompetent<sup>15</sup> template substituting the NO<sub>2</sub> with  $-\text{NH}_2$  or COOR. The C, N, and O atoms of the functional group (FG) influence both the XRD and  $\zeta$ . The sharper intensities with FP might mildly inactivate the CCA to control a scintillation that may nucleate a lattice of SIQP having FP connected to pyz and NIQ. FP has induced multiple sharper peaks with different intensities as its delocalized electron cloud is away from CCA. Thus, the NIQ and pyz could not control a split of phenyl. The harmonized  $\psi$  of pyz, FP, and NIQ generated multiple peaks via their individual oscillations at  $2\theta$ , 20–30°. FG with CN (EWG) and OCH<sub>3</sub> (ERG) have lowered the intensities by counterbalancing their electronic oscillations with SIQPII and III (Figure 3). The FP alone has sharpened a lattice vis-à-vis NIQ and pyz contrary to CN and OCH<sub>3</sub>. These have quenched the oscillations to produce the defused lattices. NIQ and pyz partitioned by CCA and tuned by FP, ERG, and EWG generate the  $e^-$  and  $h^+$  ROC for PCR activities, and a CCA maintains a continuity between the pyz and NIQ for an electronic passage. The absence of sharper electronic scintillations with CN and OCH<sub>3</sub> may infer lattice-disrupting activities of NIQ and pyz. The EWG and ERG disrupt the sharper splits compared to FP within  $2\theta \sim 20\text{--}25^\circ$ . XRD infers a disruption of SIQPI compared to NIQ alone within  $2\theta \sim 10\text{--}35^\circ$  despite its crystallinity. The NC-phenyl and 2NC-pyz units affect the electronic activities of CCA via an interconnecting C atom in response to its 1s electron. The NC-phenyl defused intensities have induced an electronic continuity via CCA (Figure 3). The CN and OCH<sub>3</sub> have developed a mild sharpness of oscillations and are unable to determine a  $d$  spacing, respectively (Table 2). The CN has shortened the  $d$  spacings with the least split so a Raman-inactive<sup>1</sup> and FT-IR-active SIQPII has lowered its polarizability, resulting in an infinite stretching. The electrolytes induced the electronic oscillations in QHIn. The higher Raman<sup>1</sup> intensities of SIQPII than I and III as 2LPE of OCH<sub>3</sub> delocalized with phenyl of III manifold the EER by weakening a polarizability. The higher continuity in XRD peaks of SIQPII than III and I is due to a slightly high activity of EWG. The NIQ alone has delocalized the

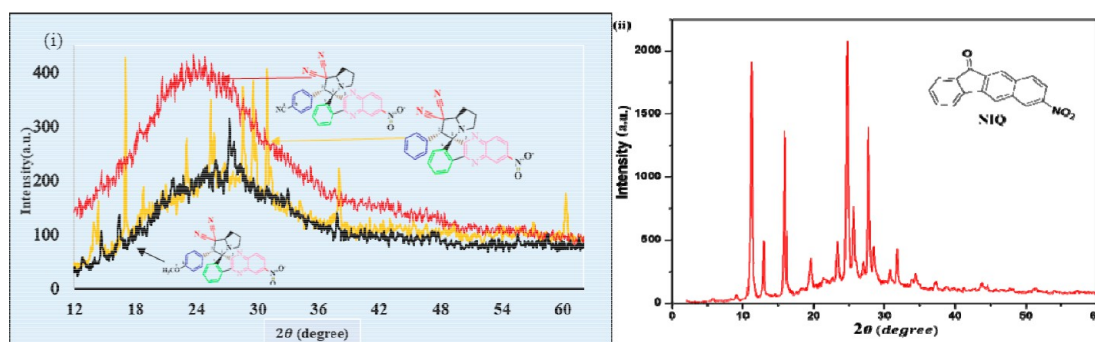


**Figure 3.** XRD intensity vs  $2\theta$  (i) SIQPs illustrating FP, EWG, and ERG and (ii) NIQ.

Table 2. XRD  $2\theta$ , Intensity, and d Spacing for SIQPs

SIQPI			SIQPII			SIQPIII		
$2\theta$ (deg)	Intensity (a.u.)	d Spacing ( $\text{\AA}$ )	$2\theta$ (deg)	Intensity (a.u.)	d Spacing ( $\text{\AA}$ )	$2\theta$ (deg)	Intensity (a.u.)	d Spacing ( $\text{\AA}$ )
8.70	45.33	5.09	8.65	103.33	5.12	6.25	43.33	7.07
14.35	162.67	3.10	14.65	219.33	3.04	8.6	58.00	5.15
17.00	427.33	2.63	18.4	308.00	2.44	14.6	104.67	3.05
23.05	278.67	1.96	23.05	422.00	1.97	16.3	127.33	2.74
25.4	350.00	1.79	23.7	434.67	1.91	22.3	194.00	2.03
25.75	289.33	1.77	24.3	424.00	1.87	25.85	231.33	1.76
28.55	374.00	1.61	24.85	429.33	1.83	27.25	314.67	1.69
29.55	384.67	1.56	25.5	417.33	1.78	27.35	268.00	1.67
29.85	262.00	1.54	29.8	331.33	1.55	32.95	181.33	1.41
30.90	406.67	1.49	30.65	298.00	1.51	37.8	134.67	1.26
31.20	220.00	1.48	35.2	219.33	1.33	47.75	94.33	1.04
38.05	223.33	1.24	57.25	118.67	0.91	55.55	94.66	0.93
60.25	176.67	0.88	69.5	94.00	0.82	58.35	96.66	0.91

electronic activities with the sharper intensities at  $2\theta = 25^\circ$ , 2000 au compared to SIQPs (Figure 3). The weakening of XRD intensities by  $\sim 88\%$  from NIQ to SIQPs with FP, CN, and  $\text{OCH}_3$  stabilize their respective oscillations. The EWG and ERG have enhanced  $\Phi$  of the dyes by minimizing a QEB,<sup>16</sup> and NIQ via CCA supports a framework of SIQP dipolar stability for generating the holes. SIQPIII with  $\text{OCH}_3$  compared to II has enhanced a sharper intensity due to  $3\sigma$  bonds and 2LPE of the O atom with a higher stability and a lowest weight (wt) loss. The SIQPs having multiple sharper peaks alignments could not produce a single lattice as the contributory units induce distinctive scintillations by aligning their charges. The SIQPs compared to NIQ ( $\sim 2000$  au) alone have stabilized their scintillating intensity as CCA has equilibrated the SIQPs (Figure 3). NIQ shows a higher melting point than SIQPs with a least wt loss<sup>1</sup> as the different functional sites via FRET equilibrated their energies. The NIQ shaper peaks infer a charge stabilization (Figure 3).

**2.3. AFM Analysis.** Functional sites are vibrantly reoriented in space with an integrated topography (Figure S3(a–c)). SIQPI topography is symmetric along a z-axis distribution forming upward ridges with an almost equal population (Figure S3(a)). The CCA of SIQPI could have aligned the NIQ, pyz, and FP with certain residual charges responding to AFM which could have localized the electron clouds and could not homogenize a topography (Figure S3(a)). Their oscillations occur with upward growth to analyze their oscillations independently or coordinately (Figure S3(a)). Thus, a surface profile interconnects a polarization of charges explained with Raman spectroscopy.<sup>1</sup> The independent FP, NIQ, and 2NC-pyz have responded to a laser to generate the  $e^-$  and  $h^+$  holes for PCR. The CCA could not integrate a topography as electronic cloud of each constituent is detained. The SIQPI topography acted as an active recipient for  $h\nu$  and  $\text{Na}^+$  and  $\text{Cl}^-$  that catalyze its functional sites acting as a cocatalyst. Hence, the  $e^-$  and  $h^+$  holes and ionic species jointly reduced a QHIn. The electronic clouds of NIQ, pyz, and NC-phenyl units interfaced with the NaCl ions to weaken the QS to PCR QHIn. The NC-phenyl had caused a topographical outward growth along the z-axis to reorient a whole topography due to  $\text{NO}_2$  and 2NC-pyz (Figure S3(b)). NC-phenyl interacted with the  $\text{Na}^+$  and  $\text{Cl}^-$  charges and also aligned the QHIn, illustrated by Raman and TGA reported previously.<sup>1</sup> The FP reoriented the SIQPI but the II aligns linearly due to NC-phenyl depicted by TGA curve. Had there been completely integrated peaks with SIQPII then the z

outward growth could have not existed. NIQ, pyz, and NC-phenyl constituents had generated the electrostatic topography of SIQPII and the ions of the NaCl had photocatalyzed the QHIn in 28 min. Hence, SIQPII was intimately aligned in a close vicinity of QHIn to minimize a QEB. The SIQPII with a maximum Raman intensity unlike I and III with the electrolytes has enhanced a PCR with high  $\Phi$ , whereas the SIQPIII having ERG had generated a robust outward growth due to a synchronization unlike II with EWG (Figure S3(b,c)). The SIQPIII with a robust upward growth has probably accumulated the electrolytes and QS taking a longer time than II for PCR. The ERG without Raman D and G peaks<sup>1</sup> did not robustly catalyze the PCR compared to EWG. The homogenized charged sites with the least surface forces of SIQPIII had generated a straight line in Raman spectra<sup>1</sup> and is self-engaged for occupying the residual forces unlike II that responds to  $h\nu$  with highest  $\Phi$ . The aligned surface charges of SIQPIII compared to II infer less crystallinity<sup>1</sup> and are FT-IR active due to bending frequencies compared to SIQPI and II. The SIQPII reengineered its functional sites with  $\text{Na}^+$  and  $\text{Cl}^-$  ions to PCR QHIn.

**2.4. FT-IR Analysis.** FP delocalizes the electron toward its center rather than a prompt response to receive  $h\nu$  delaying a PCR compared to II and III (Figure S4(a)). The CN withdraws the electron clouds from phenyl, and the  $\text{NO}_2$  withdraws the electron clouds from NIQ, so SIQPII bonds are stretched. The NC-phenyl, 2NC-pyz, and NIQ stretched in FT-IR (Figure S4(b)). The ERG and  $\text{H}_3\text{CO}$ -phenyl of SIQPIII tilt the electron cloud toward CCA while the 2NC-pyz and NIQ have counterbalanced the electronic charges (Figure S4(c)). Thus, the covalent bonds could not generate bending in FT-IR (Figure S4(c)). The sharper peaks are noticed in the bending domain with SIQPIII than II and I due to synchronization. The molecule is engaged in C–C sites rather than stretching and has negligibly induced the stretching peaks from 2250 to 4000  $\text{cm}^{-1}$  (Figure S4(c)). The bending of ERG does not favor photocatalysis and differs in FP, NC-phenyl, and  $\text{H}_3\text{CO}$ -phenyl. The photocatalyst with maximum number of EWG could lead to PCR-persistent pollutants.

**2.5. Photocatalysis Using SIQPs with Various Dyes.**  
**2.5.1. QHIn PCR with Photocatalyst SIQPs and Cocatalysts NaCl and KCl.** The  $e^-$  and  $h^+$  holes could not reduce QHIn without electrolytes as these have hydrolyzed a mixed solvent generating the  $\text{H}^+$  and  $^-\text{OH}$  and  $\psi_{\text{SIQPs}}$  and  $\psi_{\text{dyes}}$ . The 0.01 mmol SIQPs with  $0.01 \times 10^{-3}\%$   $\mu\text{g}/\text{v}$  aq-GO and 0.01874 mmol aq-MB were separately prepared for PCR. Then 0.01 mL of MB was



**Figure 4.** (a) MB PCR by 0.01 mmol of SIQPI, II, and III with GO in aq-ACN at (a)  $t = 0$  min, (b) 30 min, and (c) 110 min under SL. (b) QHIn PCR by 0.01 mmol of SIQPI, II, and III with GO in aq-ACN-EtOH at (a)  $t = 0$  min, (b) 5 min, and (c) 120 min under SL. (c) QHIn PCR by 0.01 mmol of SIQPI, II, and III with NaCl in mixed solvent at (a)  $t = 0$  min, (b) 2 min, and (c) 160 min under SL.

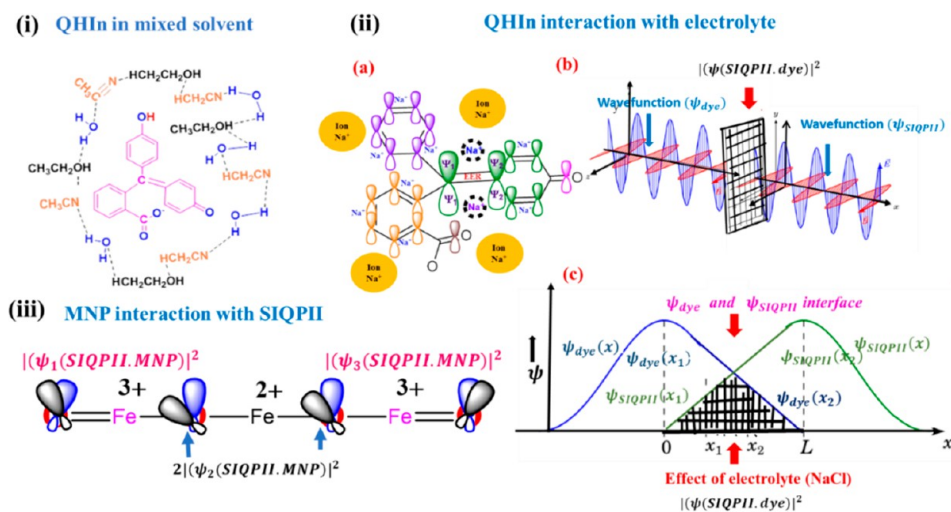


**Figure 5.** (i) Role of mixed solvent with QHIn, (ii) (a) QHIn- $\text{Na}^+$  interaction, (b, c) probability wave function  $|\psi_{\text{SIQP}II,\text{dye}}|^2$  with electrolyte of SIQP<sub>II</sub> and dye for cocatalyzing PCR, and (iii) MNPs interaction with SIQP<sub>II</sub>.

added to 5.0 mL of SIQPs with  $0.01 \times 10^{-1}$ ,  $0.01 \times 10^{-2}$ , and  $0.01 \times 10^{-3} \mu\text{g/v}$  GO solution separately. Their UV-vis absorption (abs) with  $\lambda_{\text{max}}$  and sample images before and after a PCR infer a reduction with a color change (Figure 4(a)). The 0.01 mmol SIQPs with 0.25 mL of  $0.1 \times 10^{-3} \mu\text{g/v}$  GO reduced 100% MB in <10% time than GO alone with a higher  $\Phi$  than only SIQPs (Figure 4(a)). Among  $0.1 \times 10^{-1}$ ,  $0.1 \times 10^{-2}$ , and  $0.1 \times 10^{-3} \mu\text{g/v}$  aq-GO, the  $0.1 \times 10^{-3} \mu\text{g/v}$  has

increased @PCR as free functional edges (FE) have generated a large number of  $e^-$  and  $h^+$  holes. For example,  $0.1 \times 10^{-3} \mu\text{g/v}$  GO has reduced MB in <15.15% time compared to 9.09 and 6.06% by  $0.1 \times 10^{-2}$  and  $0.1 \times 10^{-1} \mu\text{g/v}$  GO with SIQPs, respectively. GO and SIQPs upon reducing the dyes formed a brownish spongy nanocluster floating on a surface compared to GO alone which has adsorbed MB and settled within 15–30 days, and the effluents were recovered with SIQPs (Figure 4(a)).



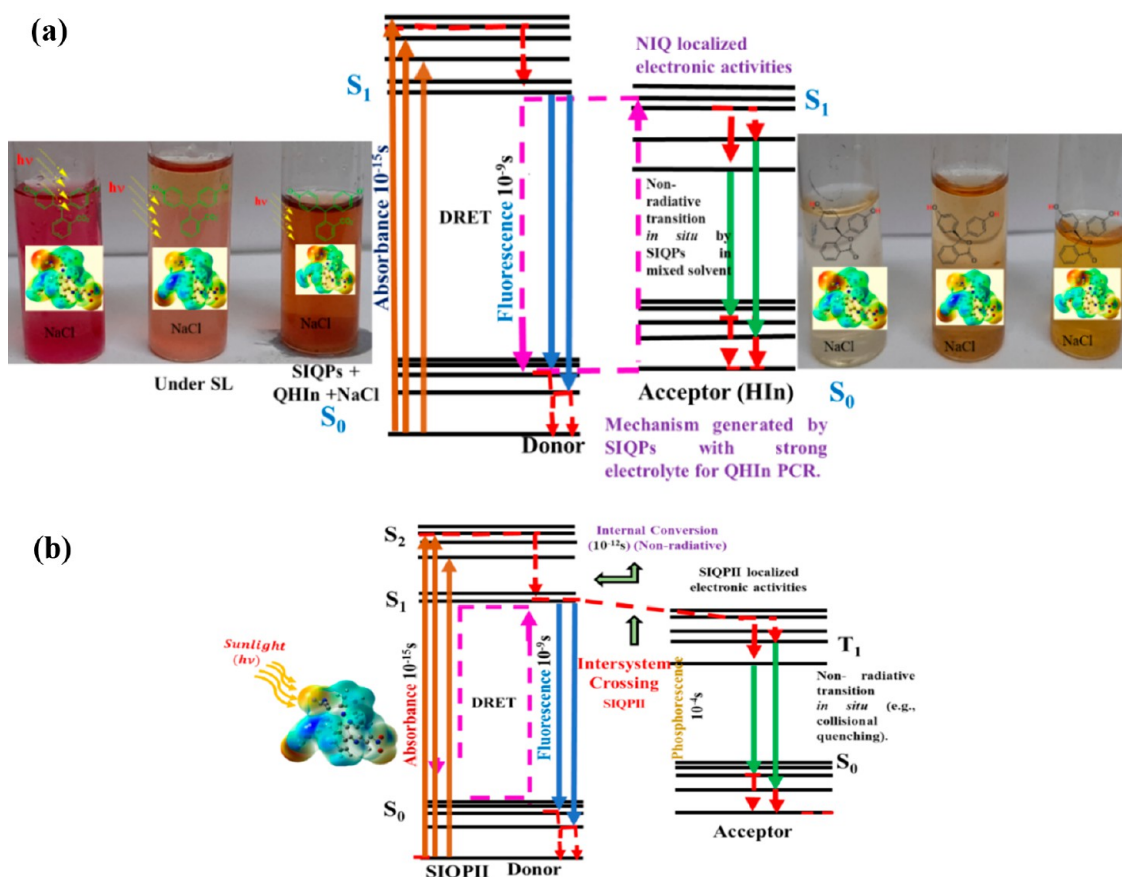


**Figure 6.** (a) DRET mechanism of SIQPs for PCR of dyes. (b) DRET with intercrossing energy system of SIQP II via a Jablonski diagram.

The absence of MB dye in effluents was confirmed by using UV–vis. GO as a photocatalyst intensified the  $\psi_{\text{SIQPs}}$  with a larger surface area (SA) on acquiring a lower activation energy ( $\Delta E_a$ ) for a higher  $\Phi$  as in eq 1.

$$SA \propto \frac{1}{\Delta E_a} SA = K_{SA} \frac{1}{\Delta E_a}, \quad SA \propto \Phi, \quad SA \propto \frac{QY}{\Delta E_a}, \quad SA = K_{SA} \frac{\Phi}{\Delta E_a} \quad (1)$$

Here,  $K_{SA}$  is the SA constant, and the monodispersed SIQPs and dyes have generated ROC using the least  $\Delta E_a$  generated holes with intense  $\psi$  and  $\pi$  conjugations that may hinder  $\psi_{\text{SIQPs}}$  (Figure S5(a)) as

$$E_\psi = \frac{p^2}{2m} \pm \frac{q_{\text{SIQPs}}^+ \times q_{\text{dye}}^-}{4\pi\epsilon r^2} \quad (2)$$

where  $E_\psi$  is the energy of ROC via  $e^-$  and  $h^+$  holes at a specific wavevector maintained a lattice, with KE ( $p^2/2m$ ), PE ( $q_{\text{SIQP}}^+ \times q_{\text{dye}}^- / 4\pi\epsilon r^2$ ) at  $r$ , nm, and  $\epsilon$  is the permittivity between the SIQP and dye (eq 2). The  $e^-$  and  $h^+$  holes of  $\psi_{\text{SIQP}}$  with GO and electrolyte reduced  $=S^+$  of MB. The SIQPs, despite bonding with the FP, CN, and  $\text{OCH}_3$  and having delocalized phenyl, one, and two nonbonding electron pairs, respectively, could not reduce the QHIn. Neither the SIQPs alone nor with GO could PCR the QHIn (Figure 4(b)). The SIQP with electrolytes monodispersed the dyes (Figure 4(c)). The QS having alternative double bonds with CCA created a lot of hindrances to minimize QEB due to their EER. The electrolyte interacts with the EER sites to attract the electron cloud toward its ionic charge (Figure 5). Hence, SIQP alone did not act as a stronger pointed charge, and the  $\text{Na}^+$  point charge undergoes EER to

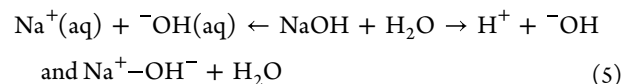
align with  $\psi_{\text{SIQPs}}$  that had destabilized the QHIn with 0.1 mmol aq-NaCl of 0.1 ionic strength ( $I$ ) as in eq 3.

$$I = \frac{1}{2} \sum C_i Z_i^2, \quad 0.1 \text{ mmol NaCl} = \text{Na}^+ = 0.1, \\ \text{Cl}^- = 0.1, \quad I = \frac{1}{2} [0.1 \times (+1)^2 + 0.1 \times (-1)^2], \quad I = 0.1 \quad (3)$$

The NaCl has weakened the double bond of QHIn and SIQPs both with a robust  $\psi_s$  developing PCI as the  $\text{OH}^- + \text{H}^+$  pushes the  $\text{Na}^+$  toward a negative charge of QHIn (Figure 5 and eq 4).

$$\text{interacting potential} = \frac{\text{QHIn} \times \text{Na}^+ \times e^-}{4\pi\epsilon r^2}, \\ \text{NaCl} \rightarrow \text{Na}^+ + \text{Cl}^-, \quad \text{NaOH} \rightarrow \text{Na}^+ + \text{HO}^- \quad (4)$$

The  $e^-$  and  $h^+$  holes reduce the residual charges of QHIn illustrated as



The  $\text{H}^+$  ion is simultaneously consumed but NaOH could not reduce QHIn. The internal exchange of the ionic species might have excited the electronic activities without interacting with the delocalized charges (eq 5). The NaCl is hydrolyzed to  $\text{NaCl} + \text{H}_2\text{O} \rightarrow \text{NaOH} + \text{HCl}$ , but NaOH with common  $\text{Na}^+$  inhibits a hydrolysis that might have disrupted the QS (eq 5). The  $\text{Cl}^-$  might have disrupted the H bonding forming anionic<sup>17</sup> hydration sphere (AHS) on the surface attracting the cation hydration sphere (CHS). These establish a closed contact of the  $e^-$  and  $h^+$  holes with QHIn. The NaCl and KCl have

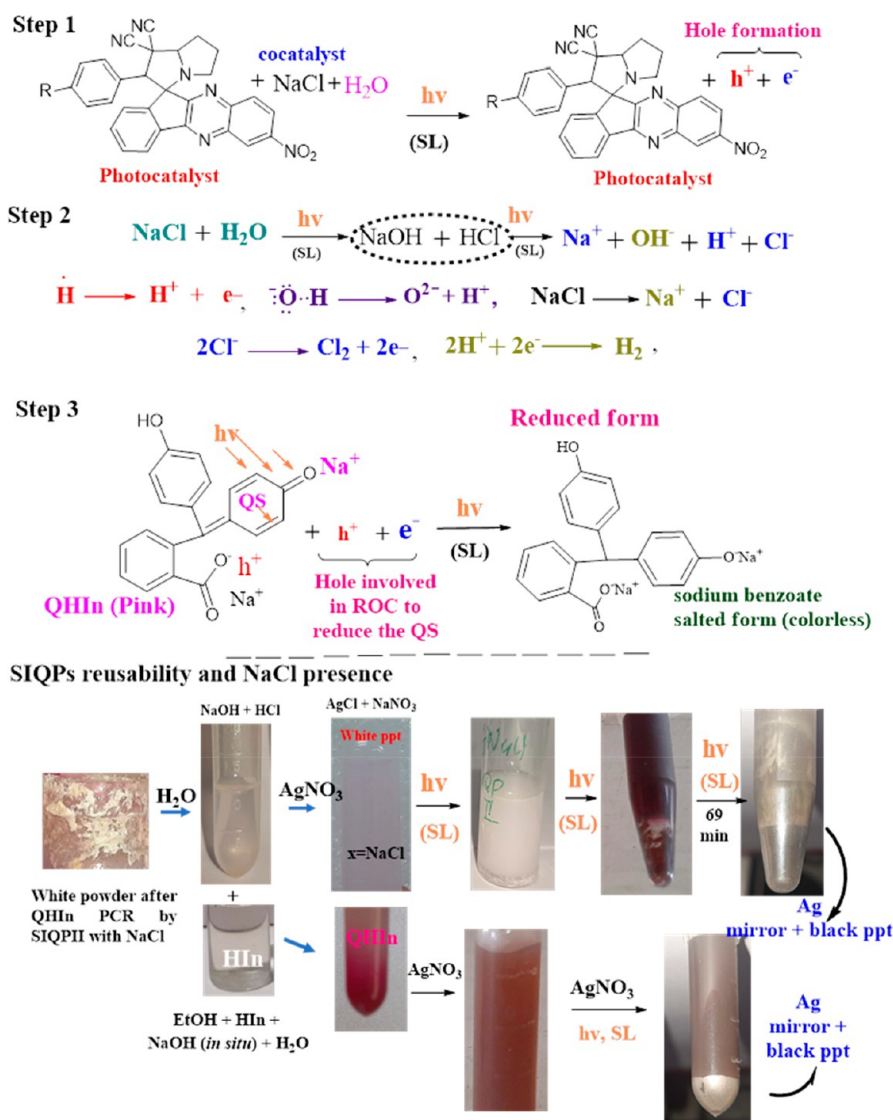
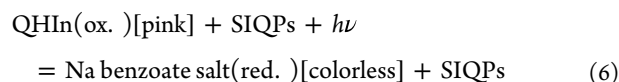


Figure 7. PCR mechanism of SIQPs to reduce QHIn under SL.

monodispersed a biphasic solvent holding aq-QHIn-NaOH at NTP by lowering  $\epsilon$  for QHIn with SIQPs. The two experiments were conducted to photocatalyze the QHIn for finding a role of QS. The SIQPs with GO reduced MB in 110, 27, and 55 min unlike 120, 45, and 70 min alone. SIQPI, II, and III with NaCl have reduced the QHIn in 120, 28, and 50 min, respectively, to PCR a persistent QHIn.<sup>18</sup> The CHS and AHS shielded a QHIn from the medium to reduce it over a longer time. The water solubilizes the EtOH and QHIn both to a single phase, and the SIQPs are soluble in ACN, developing a second phase without NaCl. The  $\text{Na}^+$  of NaOH could not disrupt the H bonding as  $\text{Na}^+$  and  $\text{Cl}^-$  had mutually monodispersed the EtOH, water, QHIn, and SIQPs to a single phase (Figure 5). The SIQPs reduced MB but not the QHIn without electrolyte as DRET failed to reduce QHIn which has no charge-deficient sites. Had the  $\text{Na}^+$  and  $\text{Cl}^-$  counterbalanced the  $\text{e}^-$  and  $\text{h}^+$  holes then there would have not been any color change on subjecting them to  $h\nu$ . So, a color disappearance on receiving  $h\nu$  infers QHIn reduction to HIn at pH 8. The  $\text{OH}^-$  and  $\text{H}^+$  produced  $\text{H}_2\text{O}$ , leaving  $\text{Na}^+$  toward  $\text{e}^-$  charged QS, but NaOH could not interfere with QHIn reduction except with SIQPs as a reducing agent. The concentrations of QHIn as an oxidizing agent and of SIQPs as a

reducing agent depend on production and consumption of  $\text{e}^-$  and  $\text{h}^+$  holes, respectively (eq 6).



The  $\text{BaCl}_2$ , a weak electrolyte, could not weaken the QS compared to a  $\text{Na}^+$  with an effective nuclear charge interacting with  $\psi_{\text{C}=\text{C}}$  of QHIn (Figure 5). Thus, an electrolyte with shorter size assists SIQPs to photocatalyze the QHIn with a small  $\Delta E_a$ . The NaCl developed PCI with QHIn and with the respective constituents of SIQPs to disrupt the H bonding (Figure 5). The KCl with similar sizes of  $\text{K}^+$  and  $\text{Cl}^-$  developed a small  $\zeta$  with comparatively weak H bonding disruption on canceling out charges on ions to reduce QHIn in 138, 58, 63 min, respectively, compared to NaCl. The  $\text{Cl}^-$ , a common anion of NaCl/KCl, could not compensate for a cationic charge. The  $\psi_{\text{CHS}}$  and  $\psi_{\text{AHS}}$  as a shorter sized  $\text{Na}^+$  with stronger nuclear charge unlike  $\text{K}^+$  weakened the QS (Figure 6(a,b)).

2.5.2. Mechanism of SIQPs to PCR the QHIn. The  $\psi$  of water and ACN accommodate hydrophilicity and hydrophobicity of SIQPs to minimize a QEB for QHIn, BBR, MO, and transition-



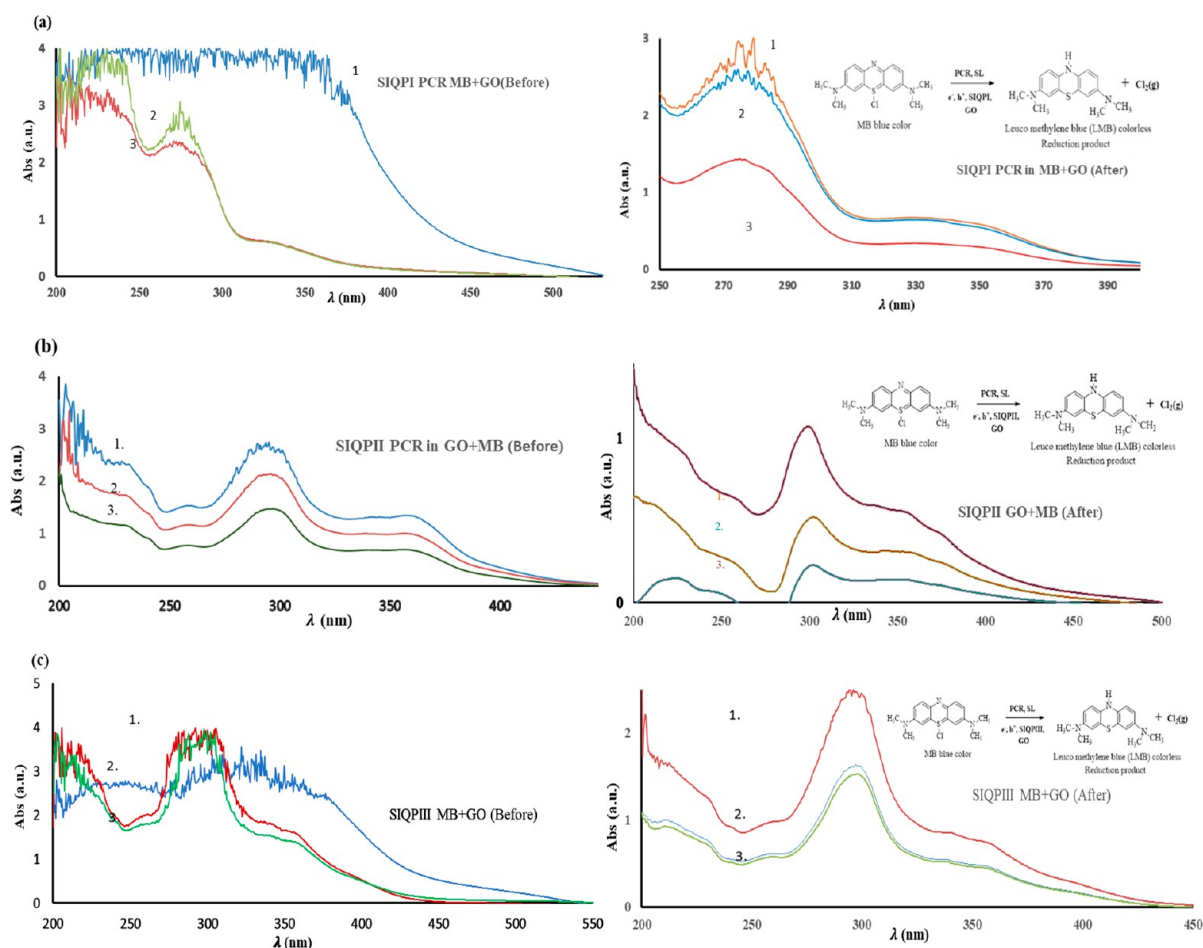


**Figure 8.** UV–vis abs before and after 110, 27, and 55 min of PCR of MB by SIQP (a) I, (b) II, and (c) III with GO of (1) 1.0 mmol, (2) 0.1 mmol, and (3) 0.01 mmol.

metal ion reduction. The  $\psi_{\text{water}}$  with  $\psi_{\text{ACN}}$  attracts the NaOH and QHIn mutually due to H bonding. The  $\text{Na}^+$  attracts  $\text{O}^{\delta 2-}$  and the  $\text{Cl}^-$  attracts  $\text{H}^{\delta +}$  of  $\text{H}_2\text{O}$  by realigning the solvents around electronically rich and deficient sites of SIQPs and QHIn. The ionic hydrations interface the SIQPs, ACN, and EtOH to develop the sheaths around SIQPs or QHIn resulting in their suspension. The cations and anions interact with QHIn, and it maintained a pink color which disappeared on PCR with SIQPs. The NaCl could not disrupt the NIQ and pyz chiral units except by disrupting a sheath of a mixed solvent around SIQPs with a small QEB (Figure 6). The QHIn with NaCl was reduced in mixed solvents of ACN,  $\text{H}_2\text{O}$ , and EtOH with 3.92, 1.84, and 1.66 D dipole moments. The  $\text{Na}^+$  and  $\text{Cl}^-$  can disrupt EER of QHIn but a nondissociating organic solvent could not disrupt EER. The  $\text{Na}^+$ , a common ion of aq-NaCl+NaOH with SIQPs, could not affect a QHIn PCR. The  $\text{OH}^-$  initiates a water split as  $2\text{H}_2\text{O} + 2\text{HO}^- \rightarrow 3\text{H}_2 + 2\text{O}_2$  where the water dipole might have generated the holes with SIQPs under  $h\nu$ . The  $\text{OH}^-$  could split  $\text{H}_2\text{O}$  into  $3\text{H}_2 + 2\text{O}_2$  to generate a pressure that had uprooted a lid of PCR vessel. Initially, the  $\text{H}^+$  consumes the  $\text{OH}^-$  that split water, so  $\text{Na}^+$  involves in PCI and the remaining NaCl settled at bottom of a PCR unit at the same pH, and the NaCl was analyzed with  $\text{AgNO}_3$  (Figure 7).

**2.5.3. UV–vis Study PCR Dyes by SIQPs with NaCl/KCl Cocatalyst and MNPs.** SIQPs with GO photocatalyzed  $\text{MB}^{\text{S}+}$  of MB (Figure 8). The ionic interactions of NaCl/KCl-QHIn-NaOH-SIQPs are analyzed under UV–vis abs to PCR QHIn

(Figures 9, 10, and S5). The 0.01 mmol each of SIQPI, II, and III have reduced 18 ppm MB with NaCl and KCl in 82, 36, and 44 min and 89, 43, and 50 min, respectively, compared to a longer time with SIQPs alone (Figures S6(a–c) and S7(a–c)). The  $h\nu$  could not disrupt QHIn and interacted with SIQPs that split  $\text{H}_2\text{O}$  into  $\text{H}^+$  and  $\text{OH}^-$  (w). The  $\text{H}^+ + \text{HO}^-$  (b)  $\rightarrow \text{H}_2\text{O}$  and  $\text{Na}^+ + \text{HO}^-$  (b)  $\rightarrow \text{NaOH}$  inhibit a common ion of NaOH ( $\text{OH}^-$  (b)). Hence,  $\text{H}^+ + \text{HO}^-$  (w)  $\rightarrow \text{H}_2\text{O}$  neutralizes NaOH so the  $h\nu$  interacted by attacking its  $\pi$  electrons. The  $e^-$  spin of the double bond of QHIn and  $\pi$  conjugated SIQPs interfaced to photocatalyze the QHIn. The robust  $\psi$  of SIQPs with MNPs ( $\text{O}=\text{Fe}^{3+}-\text{O}-\text{Fe}^{2+}-\text{O}-\text{Fe}^{3+}=\text{O}$ ) in the presence of NaCl reduced QHIn over a longer time. The magnetic field of MNPs might have either neutralized the  $e^-$  and  $h^+$  holes by restricting their movement toward QHIn or encapsulated the  $\pi$  conjugation-driven MNPs- binding with SIQPs (Figure 11). The  $e^-$  and  $h^+$  holes of GO might have mutually counterbalanced the SIQPs resulting in no photocatalysis (Figure S6 and S7). The SIQP II alone produced  $\sim 5$  times higher Raman intensities than I and III and reduced the QHIn in 28 min with electrolyte. The  $\psi_{2\text{NC-pyz}}$  interconnects the NC-phenyl via CCA of  $-\text{CH}$  of pyz where its density of energy state (DOS) restricted its alignment toward NIQ as CCA is bonded with 1C, 2C, and tertiary N atoms of pyz, respectively. The CCA with SIQP II regulates the  $\psi_{2\text{NC-pyz}}$  by mildly blocking the electron clouds of 2NC and CN for reaching NIQ to weaken the EER. Compared to 120 and 50 min for QHIn PCR by SIQPI and III,

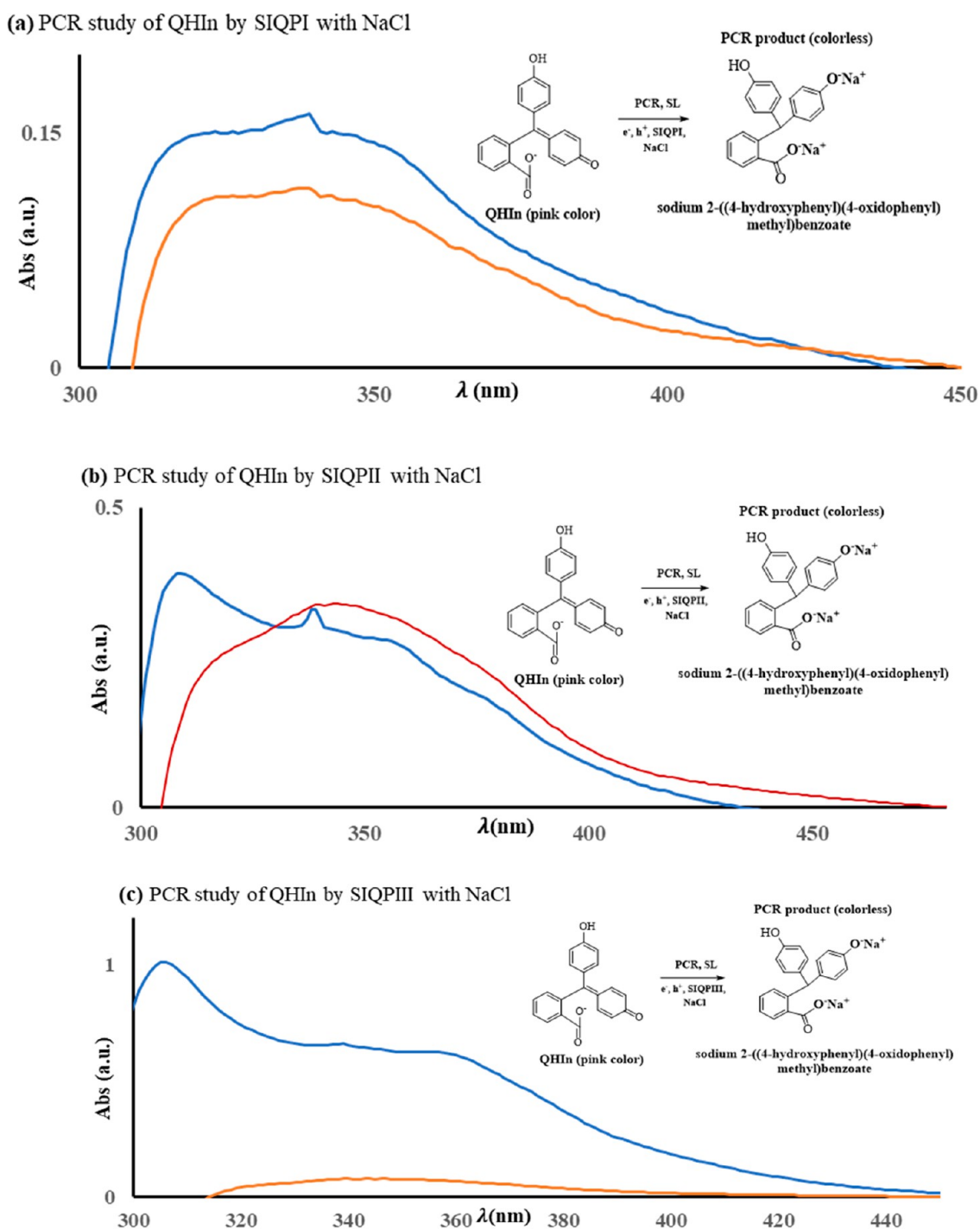


**Figure 9.** UV-vis abs of QHIn by 0.01 mmol SIQP (a) I, (b) II, and (c) III with NaCl before and after (a) 120 min, (b) 28 min, and (c) 50 min of photocatalysis.

the II has reduced in 28 min, and  $\sim 3$  times the DOS of its 2NC and CN might have mutually been interconnected with longer MFP. The 2NC and CN might have produced the maximum holes in a similar phase but still the SIQPII could not reduce QHIn (Figure 11). MNPs activated holes of the SIQPII for QHIn PCR as the  $\text{Fe}^{3+}$  and  $\text{Fe}^{2+}$  oxidation states could reorient the NC-phenyl and 2NC-pyz to reduce QHIn in a shorter time as it took 48 h instead of 28 min (Figure 11). Though the NaCl<sup>19</sup> was common in both, the MNPs have hindered a PCR of QHIn similar to an inhibition of a drug release from the trimesoyl tridimethyl malonate vehicle. MNPs with SIQPs have delayed @

PCR acting as an antiphotocatalyst, needed for stability of color coating in thin films.<sup>20</sup> The UV-vis abs by SIQPs for reducing QHIn with electrolyte KCl before and after photocatalysis are negative within 230–320 nm. As the  $\text{CH}_3\text{-C}^{\delta+}\equiv\text{N}^{\delta-}$  and  $\text{H}^{\delta+}\text{-O}^{\delta-}\text{-H}^{\delta+}$  both compete to interact with the  $\text{K}^+$  and  $\text{Cl}^-$  to disperse the QHIn and SIQPs equilibrated by  $\text{CH}_3\text{CH}_2\text{OH}$  where the  $h\nu$  of visible range reorient the QHIn and SIQPs to optimize in mixed solvent and align the dipoles on releasing the energy with transmittance >100% light on absorbing energy from a system. Thus, it attains a negative abs enhancing a PCR, as the aligned dipoles prevent a recombination of holes. The

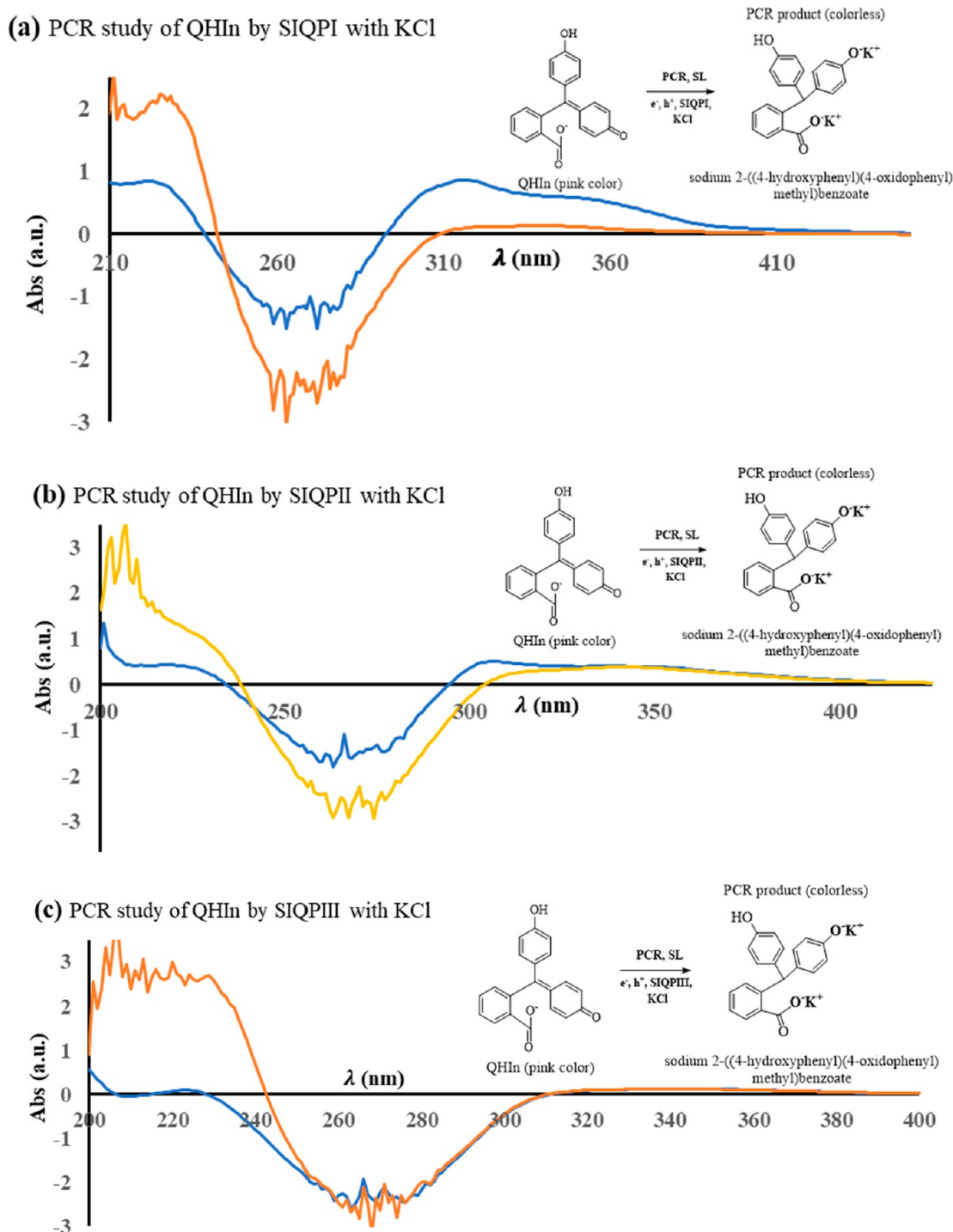


**Figure 10.** UV–vis abs of QHIn by 0.01 mmol SIQP (a) I, (b) II, and (c) III with KCl before and after (a) 138 min, (b) 58 min, and (c) 63 min of photocatalysis.

negative abs infers a constructive role of the electrolytes for enhancing a PCR. The LPE of O atoms of  $\text{H}_2\text{O}$  and  $\text{CH}_3\text{CH}_2\text{OH}$  and of the N atom of ACN expeditiously respond to the UV light upon absorbing it. The KCl is dissociated into  $\text{K}^+$  and  $\text{Cl}^-$  ions and activated a H-bonded  $\text{H}_2\text{O}$  structure, causing a transition. The LPE are embedded by KCl due to the ionic hydration spheres of  $\text{K}^+$  and  $\text{Cl}^-$  and need more energy for UV light passage. The energy released on aligning the solvents induces molecular reorientations by taking energy from the system as an endothermic process. The electrolytes via cation–

anion interactions reoriented using the energy of a system with resultant negative potential energy. No negative abs with SIQPs alone and with QHIn dispersed with mixed solvent except with electrolyte. Thereby, the solvated structure with salts inducing the maximum reorientations require exceptionally higher energy within 200–230 nm, which is taken from the system itself. It withdraws a higher energy from a medium leading to negative abs in UV. Generally, endothermic chemical processes are studied with TGA. Going forward, it could be studied with the UV light abs. The mixed solvent induces maximum reorientation



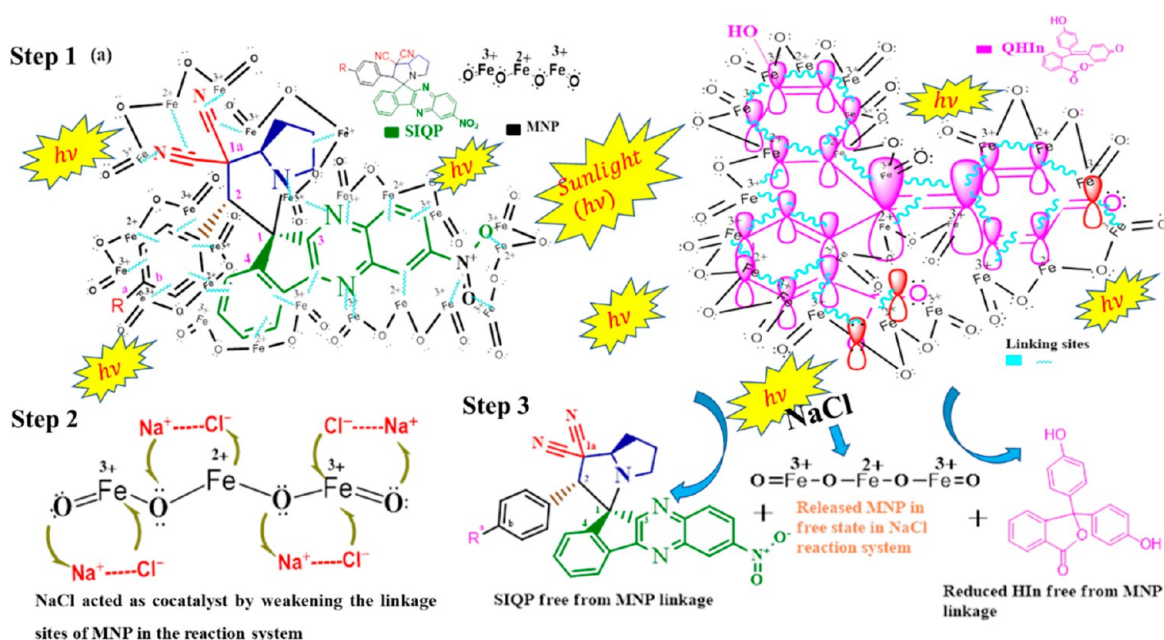


**Figure 11.** Electronic mechanism of MNPs undergoing QHIn photocatalysis by SIQPs.

motions like rotational, vibrational, and translational with the QHIn molecules vis-à-vis SIQPs as no complex formation is developed. Had a complex been developed there would have not been a PCR. The chosen mixed solvent does not coagulate, cluster, or defunct any of the molecular species. The monodispersing solvent reorients QHIn and SIQPs on utilizing a maximum energy from a medium producing a negative abs.

**2.5.4. Fluorescence Analysis.** Fluorescent<sup>1</sup> spectra produced the highest intensity ( $I_f$ ) 13995 au with SIQPII at 490 nm unlike 167 and 65 au at 490 and 489 nm with I and III. SIQPI developed a sharper and milder peak intensity due to delocalized FP. The EWG/CN SIQPII smoothed the surfaces but the ERG/OMe with III created chaos as CCA could not harmonize  $\psi$ . The cocatalysts excite electrons of QHIn and SIQPs to reduce QHIn. The fluorescence for HIn, QHIn, and electrolyte is examined with varying concentrations to study the electronic effects. Hence, at 320 nm, an excited wavelength ( $\lambda_{exc}$ ), the emitted wavelengths ( $\lambda_{em}$ ) 408, 383, 466, and 465 nm distinguish QHIn, HIn, NaCl, and KCl, respectively, via  $I_f$  and  $\Phi$  activities (Figure S8 and Table 3). Increasing the HIn concentration has produced

**Table 3. Fluorescence of SIQPI, II, and III with NaCl in Mixed Solvent ((1) 1.0 mmol, (2) 0.1 mmol, and (3) 0.01 mmol) at  $\lambda_{exc} = 320$  nm**

Product	$\lambda_{em}$ (nm)	$I_f$	$\Phi\%$ (without NaCl)	$\Phi\%$ (NaCl)
SIQPI + NaCl	417	33429	71.5	76.7
SIQPII + NaCl	423	2347751	71.5	75.6
SIQPIII + NaCl	444	2399239	71.6	72.0
SIQPII + MNPs + NaCl	501	2342932	—	73.4

sharper peaks upon increasing  $I_f$  with a stronger  $h\nu$  interaction compared to QHIn (Figure S8(a)). The sharper intensity with HIn, unlike that defused with QHIn, varies with its concentration at the same  $\lambda_{max}$  (Figure S8(b)). The diffused peaks predict the QHIn oscillations with different  $\psi$ s compared to the integrated electronic state of HIn. Hence, the photo-

catalysis to degrade the QS is justified. In QHIn spectra with the same peak of lower  $I_f$  and new broader peaks at 375–475 nm infer unphotocatalyzed QS (Figure S8(b)). The QS undergoes splits by NaCl from 400 to 650 nm that destabilize a QS at lower  $I_f$  as no split in QHIn without electrolytes occurs contrary to multiple splits with electrolytes (Figure S8(c)). These have quantized the PE to many domains with higher  $I_f$  (Figure S8(b)). The concentration trends of  $I_f$  with QHIn remained stable and changed on varying NaCl concentration. Quasi-TS (transition state (TS)) with NaCl infers anharmonic oscillations but with the KCl no split occurs except for a drastic change (Figure S8(c,d)). The shorter sized  $Na^+$  unlike a larger sized  $K^+$  has weakened a solvent bonding with QHIn due to a common  $Cl^-$  anion (Figure S8(d)). The NaCl enhanced the  $\Phi$  as a shorter  $Na^+$  induced oscillations compared to smoothing with the KCl. The charge on  $K^+$  is  $q_{K^+}$  and on the  $QS^-$  is  $q_{QS^-}$ ,

$$E = \frac{q_K^+ q_{QS^-}}{4\pi\epsilon r^2}$$
 For  $K^+$ , the  $\epsilon$  of the medium is reduced due to a large sized cation compared to  $Na^+$  where it interacted with the medium as well as with QHIn. The continuous oscillations unlike KCl have lowered the  $\epsilon$ ; however, the  $\epsilon$  with NaCl is mutually equilibrated ( $>r$ ). A quasi-TS favors the higher oscillations with NaCl than KCl. The  $\epsilon$  for the specific ratio of NaCl and KCl could further reduce a PCR time. The study is continued with a shorter sized  $Li^+$  cation having larger  $\epsilon$  to further reduce a PCR time as a large sized  $Ba^{2+}$  cation could not PCR QHIn but rather was settled. Thus, the cationic interactions contribute toward photocatalyzes QHIn. The KE with electrolytes elevated a polarity for photocatalysis, and fluorescence has illustrated their ionic actions. A single peak at 480 nm with two other peaks infers vibrant interactions of NaCl (Figure S8(c)). Fluorescence of QHIn and SIQPs inferred the induced cation selective activities with NaCl to split PE of QHIn and SIQPs for photocatalysis. The NaCl was interfaced with the SIQPs and QHIn unlike  $BaCl_2$  that did not interface a medium due to the larger  $Ba^{2+}$  size (Figure S9). The NaCl and SIQPs were recovered after PCR and were washed with chilled aq-EtOH. NaCl reduced the bandgap of QHIn and SIQPs to generate the constructive oscillations in fluorescence (Figure

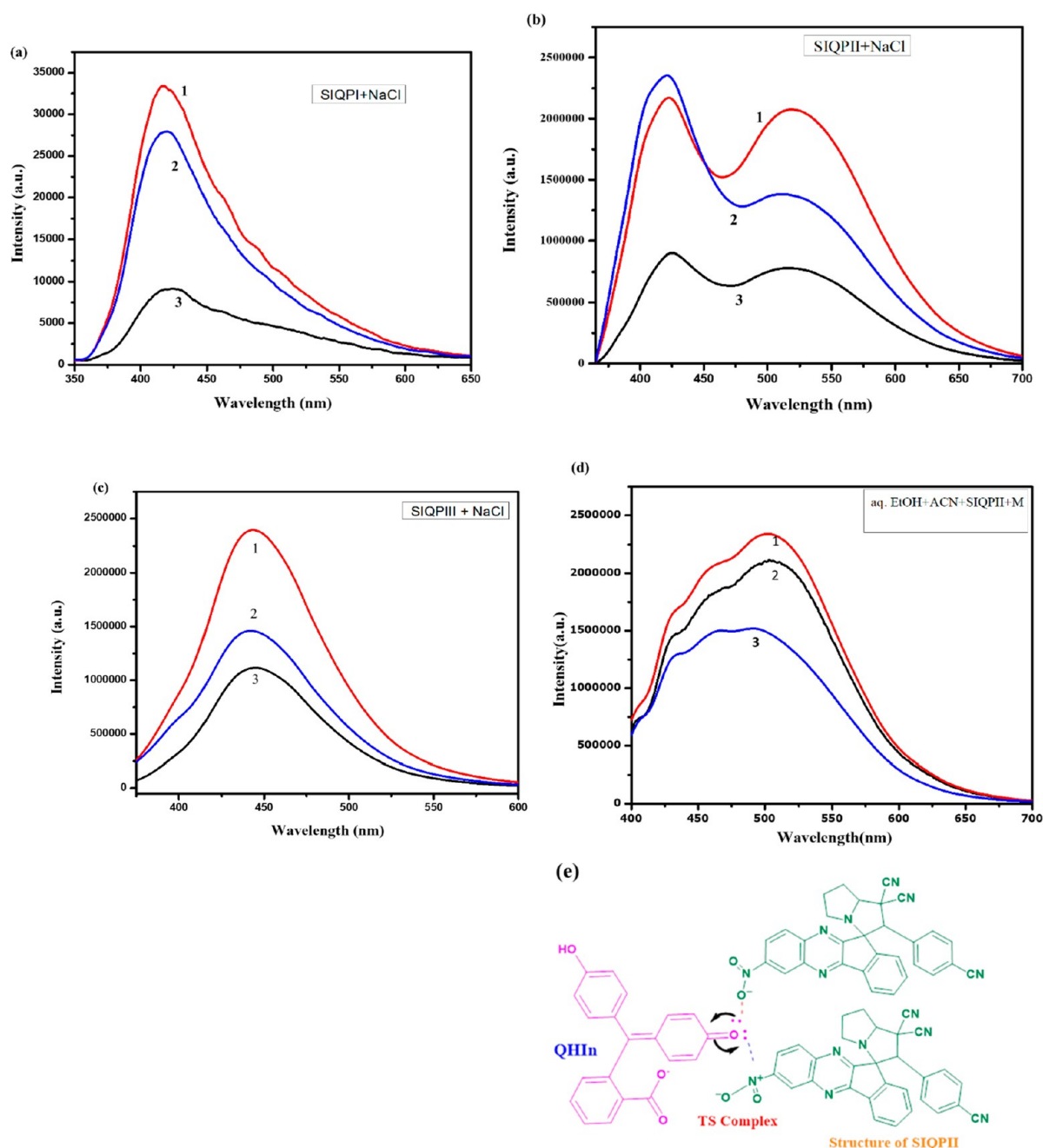


**Figure 12.** QHIn PCR using fluorescence by SIQP (a) I, (b) II, (c) III, at (1) 1.0 mmol, (2) 0.1 mmol, and (3) 0.01 mmol with NaCl and (d) SIQP II with MNPs and NaCl in mixed solvents. (e) Developing a TS by electrolytes with SIQP II to reduce QHIn.

S9). The recovered SIQPs were reused >4 times as the  $h\nu$  does not degrade them except to generate ROC. The 417, 423, 444, and 501 nm  $\lambda_{em}$  for SIQPI, II, III, and II+MNPs with NaCl, respectively, at 320 nm  $\lambda_{exc}$  compared to 489–490 nm of SIQPs alone weakened the QS with higher intensities (Figure 12). A smoothed curve at 425 nm with higher concentration favored a PCR (Figure 12(a)). NaCl with FP developed an integrated peak at 425 nm and with CN detained one peak at 425 and another at 520 nm with high  $I_f$  value. NaCl might have stressed the CCA of SIQP II producing peaks at 425 and 520 nm unlike a single peak at 425 nm with FP. The break without NaCl expands smoothly at 489 nm (Figures 12(a,b)). The SIQP II with NaCl generated a new peak due to the second transition, and it responds at 520 nm due to phosphorescence, contrary to I and III

(Figures 12(a–c) and (e)). The NC-phenyl in SIQP II expands from CN as the terminal  $\text{NO}_2$  of NIQ shifts away an electronic cloud with phosphorescence unlike FP and OMe. Thus, the TS formation with  $\text{NO}_2$  and QS of O atom decolorizes QHIn (Figure 12(e)). The OMe activity is counterbalanced by 2NC-pyz and  $\text{NO}_2$  without generating an extra peak due to interaction of the ion with the QHIn to produce a single peak (Figure 12(c)). The NaCl with SIQP II generated a phosphorescence with a conjugated QS that shortened the reduction time unlike with MNPs. The MNPs have produced a broader intensity peak and oxidation potentials of  $\text{Fe}^{2+}$  and  $\text{Fe}^{3+}$  that destabilize PCI and QS linkages with the  $\text{Na}^+$  ion (Figure 12(d)). MNPs with two oxidation potentials have caused a mild haphazardous environment that has stabilized the scintillations and could not

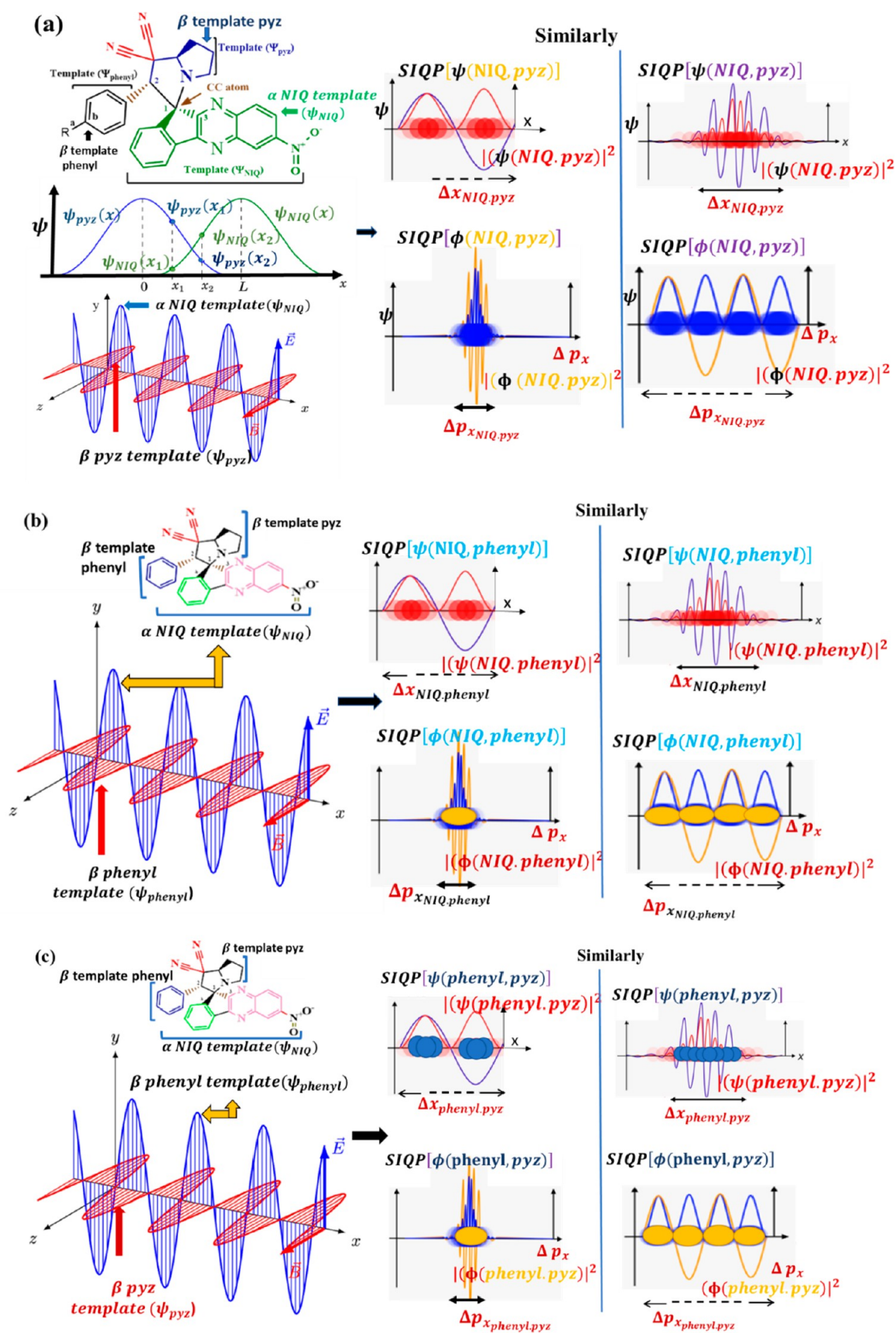


Figure 13.  $\psi$  and probability wave function  $|\psi|^2$  template interactions of (a)  $\alpha \psi_{\text{NIQ}}$  with  $\beta \psi_{\text{pyz}}$  (b)  $\beta \psi_{\text{phenyl}}$  with  $\alpha \psi_{\text{NIQ}}$  and (c)  $\beta \psi_{\text{phenyl}}$  with  $\beta \psi_{\text{pyz}}$ .



reduce a QHIn. Its terminal O atoms bonded with Fe<sup>3+</sup> produced a broader fluorescence curve due to unaligned charges (Figure 12(d)). Electronic properties of MNPs with NaCl suppressed the photocatalyzing activities on counterbalancing the oscillations. A  $h\nu$  continuous  $h\nu$  absorption could have slightly aligned the charges in 48 h, and a peak at 500 nm is sharpened and synchronized. The studies are continued with ZnO for shortening the PCR time. The  $I_f$  and  $\Phi$  for SIQP II + MNPs, SIQPI, II, and III with NaCl are calculated (Table 3). The lowest  $I_f$  values for SIQPI with NaCl than with II and III are due to symmetric  $\psi_{FP}$  (Figure 12). The NaCl with SIQP II having EWG and III having ERG caused  $\psi_{NC\text{-phenyl}}$ ,  $\psi_{H_3CO\text{-phenyl}}$  and  $\psi_{pyz}$  conjugation with  $\psi_{NIQ}$  that generated the exponential ROC contrary to I alone. EWG and ERG with electrolyte acted as fluorescent sensors (Figures 12 and 13). The  $\Phi$  at  $\lambda_{exc} = 320$  nm or  $E = 6.207 \times 10^{-19}$  J from the number of  $h\nu$  ( $n_a$ ) absorbed (eq 7) are calculated as

$$\text{no. of } h\nu \text{ absorbed } (n_a) = \frac{6.207 \times 10^{-19} \text{ J}}{6.626 \times 10^{-34} \text{ J s}}$$

$$\text{or } n_a = 0.937 \times 10^{15} \text{ s}^{-1} \quad (7)$$

The  $\lambda_{em}$  of SIQPI, II, and III at 417, 423, and 444 nm have  $4.763 \times 10^{-19}$ ,  $4.695 \times 10^{-19}$ ,  $4.473 \times 10^{-19}$ , and  $3.964 \times 10^{-19}$  J energies, respectively. For SIQPI with NaCl, the number of  $h\nu$  emitted ( $n_e$ ) are calculated with eq 8.

$$n_{e(\text{SIQPI+NaCl})} = \frac{4.763 \times 10^{-19} \text{ J}}{6.626 \times 10^{-34} \text{ J s}} = 0.718 \times 10^{15} \text{ s}^{-1} \quad (8)$$

The  $n_{e(\text{SIQP II+NaCl})}$ ,  $n_{e(\text{SIQP III+NaCl})}$ , and  $n_{e(\text{SIQP II+MNP+NaCl})}$  are calculated with eq 8 as  $n_{e(\text{SIQP II+NaCl})} = 0.578 \times 10^{15} \text{ s}^{-1}$ ,  $n_{e(\text{SIQP III+NaCl})} = 0.675 \times 10^{15} \text{ s}^{-1}$ , and  $n_{e(\text{SIQP II+MNP+NaCl})} = 0.598 \times 10^{15} \text{ s}^{-1}$ .

As  $\Phi$  is a ratio of  $n_e$  to  $n_a$ ,  $\Phi$  % for SIQPI with NaCl (eq 9) is

$$\Phi_{\text{SIQPI+NaCl}} \% = \frac{n_e}{n_a} \times 100\% = \frac{0.718 \times 10^{15} \text{ s}^{-1}}{0.937 \times 10^{15} \text{ s}^{-1}} = 76.7\% \quad (9)$$

The  $\Phi$  % for SIQP II, III, and the II+MNPs with NaCl are calculated as  $\Phi_{\text{SIQPI+NaCl}} = 76.7\%$ ,  $\Phi_{\text{SIQP II+NaCl}} = 75.6\%$ ,  $\Phi_{\text{SIQP III+NaCl}} = 72.0\%$ , and  $\Phi_{\text{SIQP II+MNP+NaCl}} = 73.4\%$  (Table 4). The  $\Phi$  % for QHIn, HIn, NaCl, and KCl are calculated with

**Table 4. Fluorescence of QHIn, HIn, NaCl, and KCl in Mixed Solvent at  $\lambda_{exc} = 320$  nm**

Product	$\lambda_{em}$ (nm)	$I_f$	$\Phi$ (%) (NaCl)
QHIn	408	88478	78.4
HIn	383	93244	83.6
NaCl	466	3569	68.8
KCl	465	12347	68.8

eq 9 as  $\Phi_{\text{QHIn}} = 78.4$ ,  $\Phi_{\text{HIn}} = 83.5$ ,  $\Phi_{\text{NaCl}} = 68.8$ , and  $\Phi_{\text{KCl}} = 68.8\%$  (Table 4). The 83.5 and 78.4% highest  $\Phi$  values with HIn and QHIn infer delocalized and QS stability, respectively. The negligible  $I_f$  values for SIQPI with NaCl reduced QHIn in 120 min as it had equilibrated the charges unlike 28 and 55 min with II and III. The NaCl potentializes SIQP functionalized with EWG and ERG, respectively. The electronically integrated SIQPI produced negligible  $I_f$  values and reduced over a longer time. The SIQPs with ERG and EWG enhanced a maximum  $I_f$  by disrupting a delocalization unlike FP. The electrolytes

vibrantly influenced the scintillations of EWG and ERG via  $\pi \rightarrow \pi^*$  and  $n \rightarrow \pi^*$  transitions; e.g., the higher  $I_f$  values for SIQP II and III compared to I with NaCl produced the highest  $\Phi$  in the same sequence of PCR with the QHIn. The CHS and AHS adhered to SIQP II and EtOH would have produced the higher electronic activities of NC-phenyl compared to I and III with FP and OCH<sub>3</sub> (Figure 13(a–c)). The NC-phenyl robustly responded to laser light and the  $\psi$  strictly infers the electronic environments of pyz and NIQ. SIQP II and III having NC-phenyl and H<sub>3</sub>CO-phenyl have generated  $\psi_{NC\text{-phenyl}}$  and  $\psi_{H_3CO\text{-phenyl}}$  as EWG and ERG activities have caused a mild stretching with pyz and NIQ (Figure 13(b,c)). The NC-phenyl with homogeneous electronic activities produced an intensified  $\psi_{\text{harmonized}}$ . The electronic environments of pyz and NIQ with SIQP II could not cope with the NC-phenyl by channelizing its energy to 2NC-pyz and NIQ via CCA. The NaCl has aligned the  $\psi_{2NC\text{-pyz}}$  and  $\psi_{NIQ}$ . The CCA with SIQP II may not support reversibility of  $\psi_{NC\text{-phenyl}} \neq \psi_{2NC\text{-pyz}} \neq \psi_{NIQ}$  mutually due to different electronic states that attract the NaCl (Figure 13(b)). The CCA as a stabilizer with higher PE and lower KE led to

$$E = \frac{p^2}{2m} - \frac{q^+q^-}{4\pi\epsilon r^2} \quad (10)$$

With CCA, the KE = 0, so eq 10 becomes  $E = \frac{q^+q^-}{4\pi\epsilon r^2}$ . The energy ( $E$ ) could be of pyz and NIQ as a NaCl with respective ions stabilizes the secondary and tertiary TS with deficient electronic oscillations. The NC-phenyl acted as the ground state ( $S_0$ ) and the CCA as the secondary state ( $S_1$ ) to optimize a tertiary ( $S_2$ ) state (Figure 13(b)). The CCA  $\approx$  NIQ could generate  $S_2$  which might be supported by CCA  $\approx$  pyz to develop a full fledged electronic system based on Schrodinger's eq 10 rearranged with KE > PE as eq 11.

$$E = \frac{p^2}{2m} \text{ or } \frac{h^2}{2m} - \frac{q^+q^-}{4\pi\epsilon r^2}, \text{ where } \left(\frac{h^2}{2m}\right) > \left(\frac{q^+q^-}{4\pi\epsilon r^2}\right) \quad (11)$$

Stretching  $S_2$  emits electron as its PE is converted in KE due to HOMO  $\rightarrow$  LUMO to equilibrate  $\psi$  of SIQPs expressed as NIQ  $\approx$  CCA  $\approx$  pyz.

**2.5.5. PCR of BBR by SIQPs.** SIQPs have reduced 100% MB and BBR despite a double number of conjugated rings with BBR compared to MB. Initially, a blue color of BBR with SIQPI and II in aq-ACN reduced to colorless after 62 and 46 min, respectively (Figure 14 and Table 5). The SIQP III with an O atom of OCH<sub>3</sub> took a longer time as its electron-releasing activities caused EER with a delocalized phenyl ring influencing both the pyz and NIQ templates. The BBR with  $\pi$ -conjugated rings created a center to receive the  $h\nu$  and created the possibility of energy loss. It activates the centers that do not resonate with the same energy and may lead to EER and the SIQP III having OCH<sub>3</sub> and BBR with delocalized rings, ethyl groups, with two SO<sub>3</sub><sup>2-</sup> delayed @ PCR. The quaternary N with alternative double bonds of BBR and a CCA delayed a PCR affecting an overall delocalization. The BBR with an active core center activates all three different sites. A delocalization is extended to periphery, probably many electronic sensitive sites on receiving  $h\nu$  from SIQP III reorient, align, and oscillate to acquire energy for PCR. Unlike MB, the BBR with a flexible electronic configuration does not act as a harmonic oscillator with different  $\psi$ . Thereby, most of the energy received by SIQP III is transferred to BBR on a resonating  $\psi$  as it aligns and reorient to PCR a dye. The complicated

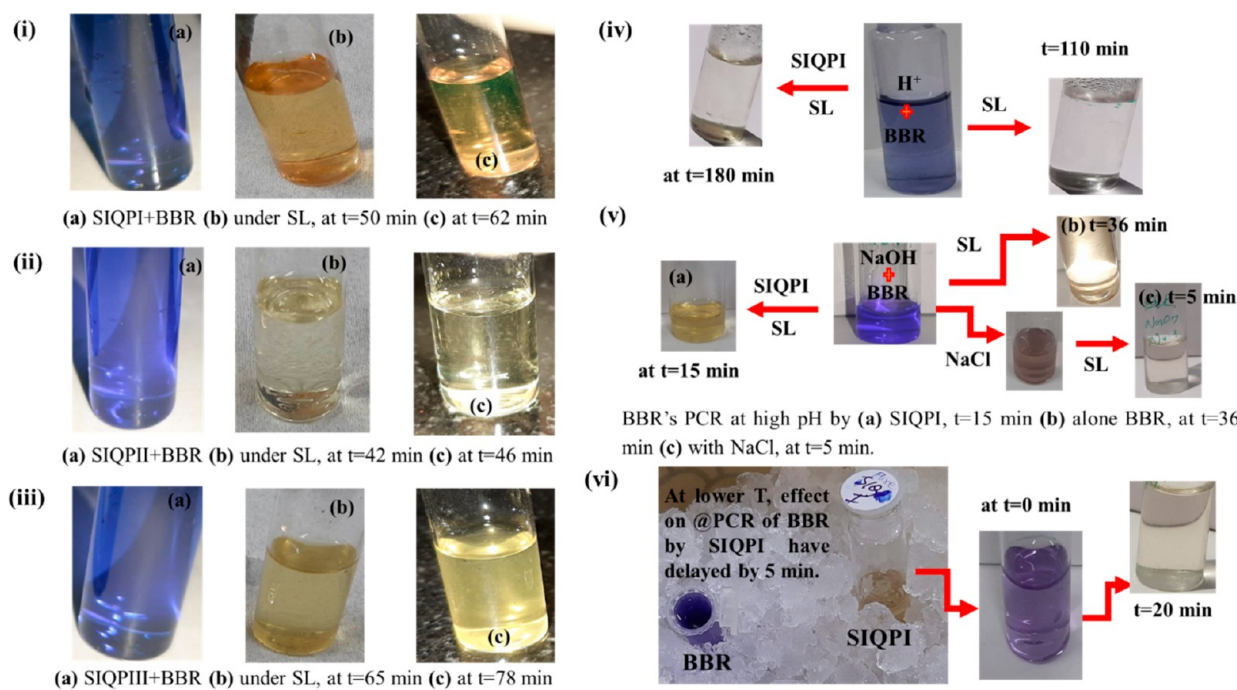


**Figure 14.** BBR photocatalysis at variable conditions with and without SIQPs.

electronic sites of BBR with SIQPIII are reduced in 78 min. SIQPs with BBR have generated a pressure inside a PCR vessel to split  $\text{H}_2\text{O}$  as  $2\text{H}_2\text{O} \rightarrow 4\text{H}^+ + 2\text{O}_2^{2-}$ , or  $4\text{H}^+ + 4e^- \rightarrow 2\text{H}_2$ , and  $2\text{O}_2^{2-} + 4\text{H}^+ \rightarrow \text{O}_2$ . The more hydrophobic BBR compared to MB<sup>1</sup> has double conjugated phenyl rings with ethyl group where the SIQPIII senses a hydrophobicity. With SIQPI and II, the water split into  $\text{H}_2$  and  $\text{O}_2$  had generated a pressure, but a robust water split occurred with III. SIQPIII, a hydrophobic sensor, delayed a PCR of BBR. Compared to SIQPIII, I and II could not sense a hydrophobicity of BBR as it is active due to ERG and quaternary N for water solubility. With BBR as a hydrophobic dye, the SIQPIII enhanced photocatalytic activity on exchanging resonating energy. The six conjugated rings in BBR with hydrophobic–hydrophobic resonance energy generate a harmonized  $\psi$ . The  $\psi$  of a hydrophobic species may resonate in a same phase to minimize QEB. The conjugating units having electron pairs with one quaternary N atom at a periphery of active core center and ERG  $\text{OCH}_3$  delayed a @PCR with SIQPIII.

**The pH (4 and 8) and T Effect on PCR of BBR by SIQPI.** Aq-BBR alone at pH 4 was reduced in 110 min unlike 180 min with SIQPI and acted as a negative photocatalyst (Figure 14 and Table 5). The BBR and SIQPI with their respective FGs and  $\pi$  conjugation might have engaged the  $e^-$  receiving centers for generating a hole mechanism. aq-BBR alone at low pH received  $h\nu$  directly and was reduced in a shorter time due to the  $\pi$  conjugation sites. Their  $\pi$  conjugated rings with two ethyls, a delocalized ring, and electron-deficient N might have developed the resonating holes. The blue color of aq-BBR at low pH disappeared in 110 min as the  $\text{H}^+$  ions have replaced its  $\text{Na}^+$  of  $\text{SO}_3^{2-}$ . The  $\text{Na}^+$  might have interacted with the  $\text{Cl}^-$  of BBR, and the  $e^-$  holes interacted with its quaternary N atom where a double bond of delocalized ring might have shifted toward a quaternary N atom. Also, the  $\text{Na}^+$  could have developed the PCI to disrupt the delocalized ring of BBR. The SIQPI with BBR seems to hold the  $\text{H}^+$  ions by H bonding with its  $\text{NO}_2$  and  $\pi$  conjugated  $e^-$  clouds resonating in different phases. No  $\text{H}^+$  ion is

free to hold the electronic sites of BBR and could not destabilize the quaternary N atom. The  $\pi$  conjugated systems with FEs of BBR and SIQPI both could have mutually doped and develop a stable nanocluster. Thus, the SIQPI and BBR mutually might have generated the resonating energy forming a compact nanocluster and aligns their electronic configuration that remained suspended homogeneously in water (Figure 14). Thus, the SIQPI and BBR might have developed the electronic linkages resisting PCR activities. The  $h\nu$  could not be absorbed by a nanocluster, so the SIQPI acted partially as an adsorbent than a photocatalyst at a pH 4.

**T Effect on BBR PCR.** The SIQPI at  $\sim 3^\circ\text{C}$  reduced the BBR over a longer time. At  $\sim 3^\circ\text{C}$ , a milder resonating energy of SIQPI developed a weak  $\psi$  so a higher  $E_a$  is needed to resonate  $\psi$  and PCR. It has delayed a PCR process ( $\sim 5$  min) to overcome QEB contrary to a shorter time. At pH 8, a BBR alone was reduced in 36 min compared 15 min with SIQPI. The BBR with SIQPI at normal T and pH 8 was reduced in 15 min compared to 20 min at  $\sim 3^\circ\text{C}$  (Figure 14). The T catalyzes the generation of holes; however, the SIQPI with NaCl at pH 8 was photocatalyzed aq-BBR in 5 min. Hence, a NaCl reduced a dye in 1/4 the time. Therefore, a catalysis of dye with electrolyte is a greener route where the  $\text{Na}^+$  attacks the  $\text{Cl}^-$  of quaternary N as well as initiates the PCI with their  $\pi$  conjugated systems. The  $\text{OH}^-$  controls a PCR of BBR by destabilizing a structured solvent and PCI. At lower pH, either a free radical or water could have split as  $\text{H}_2\text{O} \rightarrow 2\text{H}^+ + \text{O}_2^{2-}$ . At pH 4, a water splitting could have been inhibited due to a common  $\text{H}^+$  ion unlike at pH 8, so it is an essential mechanism at low and high pH due to  $\text{H}^+$  ion concentration. For adsorbing any industrial dye by SIQPs, a pH range is a prerequisite with SIQPs photocatalysts under SL at pH 4. The  $\text{Na}^+$ , a common ion at pH 8, did not affect PCR unlike at pH 4. The SIQP as photocatalyst and NaCl as a cocatalyst at higher pH enhanced the T oscillation the electron where the  $\text{Na}^+$  and  $\text{Cl}^-$  catalysis generation is due to the electronic environment around the SIQPs.

Table 5. QHIn, MB, BBR, MO, and Transition-Metal Salts PCR by SIQPs under Variable Conditions and Some Other Reported Catalysts

Solvent System for PCR Study	Sample Solution Used for PCR	pH/Color of Litmus	Reduction Time (min)	% PCR	Photocatalyst/Cocatalyst/Quencher
<b>This Work</b>					
<b>QHIn PCR by SIQPs with NaCl/KCl and MNPs</b>					
Aq-ACN	SIQPI+QHIn+NaCl	Blue	120	100%	Photocatalyst = SIQPI
Aq-ACN	SIQPPII+QHIn + NaCl	Blue	28	100%	Photocatalyst = SIQPPII
Aq-ACN	SIQPPIII+QHIn+NaCl	Blue	50	100%	Photocatalyst = SIQPPIII
Aq-ACN	SIQPPII+QHIn + NaCl+MNPs	Blue	2880	100%	Photocatalyst = SIQPPII
Aq-ACN	SIQPI+QHIn+KCl	Blue	138	100%	Photocatalyst = SIQPI
Aq-ACN	SIQPPII+QHIn+KCl	Blue	58	100%	Photocatalyst = SIQPPII
Aq-ACN	SIQPPIII+QHIn+KCl	Blue	63	100%	Photocatalyst = SIQPPIII
<b>MB PCR by SIQPs</b>					
Aq-ACN	SIQPI+MB	Blue	120	100%	Photocatalyst = SIQPI
Aq-ACN	SIQPPII+MB	Blue	45	100%	Photocatalyst = SIQPPII
Aq-ACN	SIQPPIII+MB	Blue	70	100%	Photocatalyst = SIQPPIII
<b>MB PCR by SIQPs with GO</b>					
Aq-ACN	SIQPI+MB+GO	Blue	110	100%	Photocatalyst = SIQPI
Aq-ACN	SIQPPII+MB+GO	Blue	27	100%	Photocatalyst = SIQPPII
Aq-ACN	SIQPPIII+MB+GO	Blue	55	100%	Photocatalyst = SIQPPIII
<b>BBR PCR with and without SIQPs and NaCl</b>					
Aq-ACN	SIQPI+BBR	pH = 7	62	100%	Photocatalyst = SIQPI
Aq-ACN	SIQPPII+BBR	pH = 7	46	100%	Photocatalyst = SIQPPII
Aq-ACN	SIQPPIII+BBR	pH = 7	78	100%	Photocatalyst = SIQPPIII
Aq	Alone BBR	pH = 4	110	100%	Quencher= medium
Aq-ACN	BBR+SIQPI	pH = 4	180	100%	Photocatalyst = SIQPI and Quencher = medium
Aq	Alone BBR	pH = 8	36	100%	Cocatalyst = NaCl
Aq-ACN	BBR+SIQPI	pH = 8	15	100%	Photocatalyst = SIQPI and Cocatalyst = medium
Aq-ACN	BBR+SIQPI+NaCl	pH = 8	5	100%	Cocatalyst = NaCl
Aq-ACN	BBR+SIQPI, at low T (ice bath)	pH = 8	20	100%	Quencher= low T
<b>MO PCR with and without SIQPs and NaCl</b>					
Aq	0.01 (M) MO+NaOH	pH = 8	60	100%	-
Aq-ACN	SIQPI+MO	pH = 8	33	100%	Photocatalyst = SIQPI
Aq-ACN	SIQPPII+MO	pH = 8	25	100%	Photocatalyst = SIQPPII
Aq-ACN	SIQPPIII+MO	pH = 8	5	100%	Photocatalyst = SIQPPIII
Aq-ACN	SIQPI+MO+0.01 (M) NaCl	pH = 8	19	100%	Photocatalyst = SIQPI and Cocatalyst = NaCl
Aq-ACN	SIQPPII+MO+0.01 (M) NaCl	pH = 8	12	100%	Photocatalyst = SIQPPII and Cocatalyst = NaCl
Aq-ACN	SIQPPIII+MO+0.01 (M) NaCl	pH = 8	~1–2	100%	Photocatalyst = SIQPPIII and Cocatalyst = NaCl
<b>Transition-Metal Salts PCR with and without SIQPs and NaCl</b>					
Aq-ACN	SIQPPII+aq-NiCl <sub>2</sub>	Neutral	38 h	~80%	Photocatalyst = SIQPPII
Aq-ACN	SIQPPII+aq-CrO <sub>2</sub>	Neutral	200	100%	Photocatalyst = SIQPPII
Aq-ACN	SIQPPII+aq-KMnO <sub>4</sub>	Neutral	30	100%	Photocatalyst = SIQPPII
Aq-ACN	SIQPPII+aq-CuSO <sub>4</sub>	Neutral	18 h	~80%	Photocatalyst = SIQPPII
Aq-ACN	SIQPPII+aq-MnCl <sub>2</sub>	Neutral	69	100%	Photocatalyst = SIQPPII
<b>Other Reported Catalytic/PCR Using MOF/Coordination Polymer</b>					
Aq- <i>n</i> -hexane	NaBH <sub>4</sub> + Ni/MIL-53				Catalyst = Ni/MIL-53
	NaBH <sub>4</sub> + Ni/MIL-53–Al <sub>2</sub> O <sub>3</sub>				Catalyst = Ni/MIL-53–Al <sub>2</sub> O <sub>3</sub>
Aq	{[Pb(Tab) <sub>2</sub> (PF <sub>6</sub> ) <sub>4</sub> ] <sub>n</sub> (1) + MO dye	-	360 min	~97%	Photocatalyst = (1)
Aq	{[Pb(Tab) <sub>2</sub> (bpe)] <sub>2</sub> (PF <sub>6</sub> ) <sub>4</sub> ] <sub>n</sub> (2) + MO dye	-	300 min	~97%	Photocatalyst= (2)
Aq	{[Pb(Tab) <sub>2</sub> (bpe)] <sub>2</sub> (PF <sub>6</sub> ) <sub>4</sub> .1.64AgNO <sub>3</sub> ] <sub>n</sub> (2a) + MO dye	-	50 min	~97%	Photocatalyst= (2a)
Aq	Ag <sub>2</sub> O–Bi <sub>2</sub> O <sub>3</sub> + MO	-	60 min	78%	Photocatalyst= Ag <sub>2</sub> O–Bi <sub>2</sub> O <sub>3</sub>

2.5.6. PCR of MO with SIQPs at pH 8. The SIQPs to PCR a MO at pH 8 resonate their sites, for example, SIQPI with MO in aq-NaOH was PCR in 60 min unlike 33, 25, and 5 min with SIQPI, II, and III (Figure 15). The SIQPs with MO increased a delocalization by shortening the PCR time. The 0.02 mL of 0.01

M NaCl with SIQPI, II, and III individually has further lowered the MO reduction time to 19, 12, and ~1–2 min (Table 5). The electrolytes monodispersed at pH 8 for a better response of *hν*. The Na<sup>+</sup> of NaCl and a Na<sup>+</sup> of NaOH might have counterbalanced a pH effect. Thus, the MO was degraded in



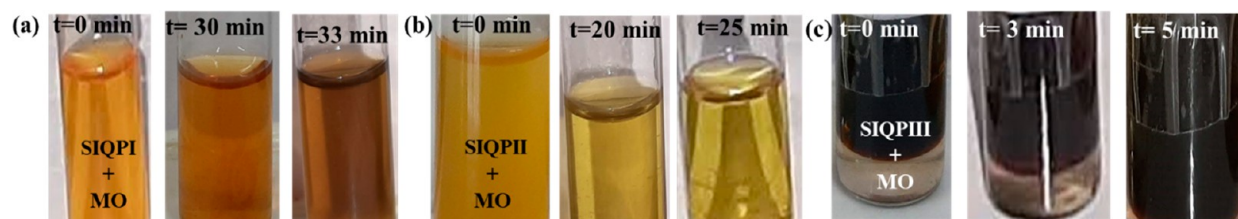


**Figure 15.** MO photocatalysis in aq-ACN by (a) SIQPI+MO, (b) SIQPPI+MO, and (c) SIQPIII+MO at pH 8 at different time.

**Table 6.** Advancement of SIQPs Photocatalysts over Reported Photocatalysts for PCR of Dye

This Work	Reported Work
1. SIQPs with electrolytes reduce effectively, are washable, reusable for more than 4 times.	1. Not washable, lower reducing efficiency, not reusable, do not reduce persistent pollutant even with electrolytes.
2. SIQPs with electrolytes reduce persistent pollutants.	2. No study with stronger electrolytes is reported yet as they could damage photocatalysing activity.
3. Highly compatible with electrolytes to reduce dyes even in presence of salt impurities.	3. They are highly pH sensitive and have limitations to degrade at high or low pH.
4. SIQPs have reduced QHIn, BBR, MO, and MB at wider pH without degradation.	4. At high $T$ as metal ligands or complexes are not stable and unfavorable for PCR.

5–33 min by SIQPs with 100% compared to in 360 min with 97% with  $\{[\text{Pb}(\text{Tab})_2]_2(\text{PF}_6)_4\}_n$  reported catalysts<sup>21–23</sup> (Table 6). SIQPs are highly stable at high  $T$  compared to the metal complexes. The metal complexes are not recycled for reuse as they undergo structural transition by losing photocatalysis abilities as compared in Table 6. SIQPs have reduced QHIn, BBR, and MO and were maintained structurally with the reducing activities for receiving the  $h\nu$  at various  $T$  and pH. The SIQPs have worked with several solvents like ACN, aq-ACN, and aq-ACN-EtOH with electrolytic solutions enhancing PCR of dyes. SIQPs were reused for four successive cycles to degrade the persistent pollutant due to their survival. The SIQPs worked without acquiring any transitional/structural changes. SIQPs have physisorbed the dyes without chemisorption on reduction so their surface area and surface energy remained almost the same in each reusable step. Their PCI interactions with NaCl, KCl, and MNPs are weak and do not concentrate the negative electronic charges on the benzene ring of SIQPs. The EWG regulates the PCI interactions with any of the ions, and their electronic cloud is not nucleated to a center. The PCI could develop with QHIn but not with CCA having different functional units. The CCA seems to generate the anti-PCI activities to avoid their degradation. The SIQPs as novel photocatalysts reduce the dyes in the presence of NaCl, KCl, and MNPs by maintaining a maximum  $h\nu$  receiving activity. The MNPs were settled at the bottom but with electrolytes were dispersed. Thus, the SIQPs did not participate in the disruption of medium linkages with a least solvent–MNPs interaction. The MNPs were phased out and could not communicate with dye and remained unengaged, but with electrolytes, their different oxidation states equilibrated with respect to oxygen. The SIQP could not disperse the MNPs as the SIQPs structure is integrated via CCA. The SIQPs have developed an extended conjugated electronic cloud throughout a molecule. Thus, there is no SIQPs interaction between medium and dyes rather than developing the PCR activity with electrolytes without SIQPs degradation. SIQPs with increasing concentrations linearly increase the intensity in fluorescence confirming their non-degradation.

**2.5.7. PCR of Transition Metal Salts with SIQPs.** Aq-NiCl<sub>2</sub> (light green), aq-CrO<sub>3</sub> (red), aq-KMnO<sub>4</sub> (purple), aq-CuSO<sub>4</sub> (blue), and aq-MnCl<sub>2</sub> (light pink) were reduced by SIQPPI with

a highest @PCR due to its N≡C-phenyl (Figure 16). The transition-metal ions caged with ionic hydration spheres interfered with a PCR. The caging was disrupted by sonication for a specific period and  $T$  at @30 kHz. Their UV–vis were recorded at initial and final stages for calculating the  $E_a$  with Arrhenius eq 12.

$$\log(\text{abs}) = \log A - \frac{E_a}{2.303R} \frac{1}{t_{\text{soni}}} \quad (12)$$

The  $A$  is the pre-exponential factor as  $h\nu$  generated by SIQPPI to reduce the metal ions or form a MOF,<sup>24</sup>  $R = 8.314 \text{ J mol}^{-1} \text{ K}^{-1}$ , and  $t_{\text{soni}}$  is sonicated time.  $\text{Abs} = f(t_{\text{soni}})$  is plotted vs  $(1/t_{\text{soni}})$  with  $E_a/2.303R$  as the slope value and the  $R$  value, the  $E_a$  is calculated with eq 13.

$$\text{slope value} = \frac{E_a}{2.303R} \text{ or } E_a = -2.303 \times 8.314 \times \text{slope values}$$

The  $E_a$  (J/mol) is calculated as (KMnO<sub>4</sub>+SIQPPI) 1822.00 > (CrO<sub>3</sub>+SIQPPI) 1315.65 > (MnCl<sub>2</sub>+SIQPPI) 556.34 > (CuSO<sub>4</sub>+SIQPPI) 419.37 > (NiCl<sub>2</sub>+SIQPPI) 349.22 and infers a higher  $E_a$  for aq-KMnO<sub>4</sub>+SIQPPI than other transition-metal ions (Figure 17). The trend infers a lower activity due to 4O<sup>2-</sup> with K<sup>+</sup> and Mn<sup>7+</sup>, and the Mn<sup>7+</sup> is reduced to Mn<sup>2+</sup> of black color. The O<sup>2-</sup> anion released electrons to reduce Mn<sup>7+</sup> + 5e<sup>-</sup> → Mn<sup>2+</sup> + 2e<sup>-</sup> → Mn<sup>0</sup> as an *in situ* double reduction process. Thus, reduction of KMnO<sub>4</sub> has utilized an evolved energy to PCR in 30 min unlike other transition metals. The e<sup>-</sup> holes generated by SIQPPI convert a nascent O atom to O<sub>2</sub> that generated a high pressure and opened the lid of a PCR vessel. The SIQPPI reduced KMnO<sub>4</sub> to prepare the Mn NPs as Mn<sup>7+</sup> + 5e<sup>-</sup> → Mn<sup>2+</sup> + 2e<sup>-</sup> → Mn<sup>0</sup> and formed nascent O atom from O<sup>2-</sup> electrons. The O atom quickly received the e<sup>-</sup> holes so a SIQPPI did not allow a reversible reaction of KMnO<sub>4</sub>. The second highest  $E_a$  for CrO<sub>3</sub> infers a stronger chemical activity due to a lower number of O atoms with a single Cr<sup>6+</sup> unlike 4O<sup>2-</sup>, K<sup>+</sup>, and Mn<sup>7+</sup> of KMnO<sub>4</sub>. Initially, the SIQPPI with CrO<sub>3</sub> produced a red turbidity that transformed to a brown color in SL and settled at the bottom. The central Cr<sup>6+</sup> (4s<sup>0</sup> 3d<sup>0</sup>) shared its valence d electrons and got adsorbed with SIQPPI to develop a MOF. The SIQPPI adsorbed the Cr<sup>6+</sup> pollutants from industrial wastes.<sup>25</sup> In addition, the MnCl<sub>2</sub> with Mn<sup>2+</sup> with d<sup>5</sup> is stable and has developed MOF of a dark gray color and was settled at the

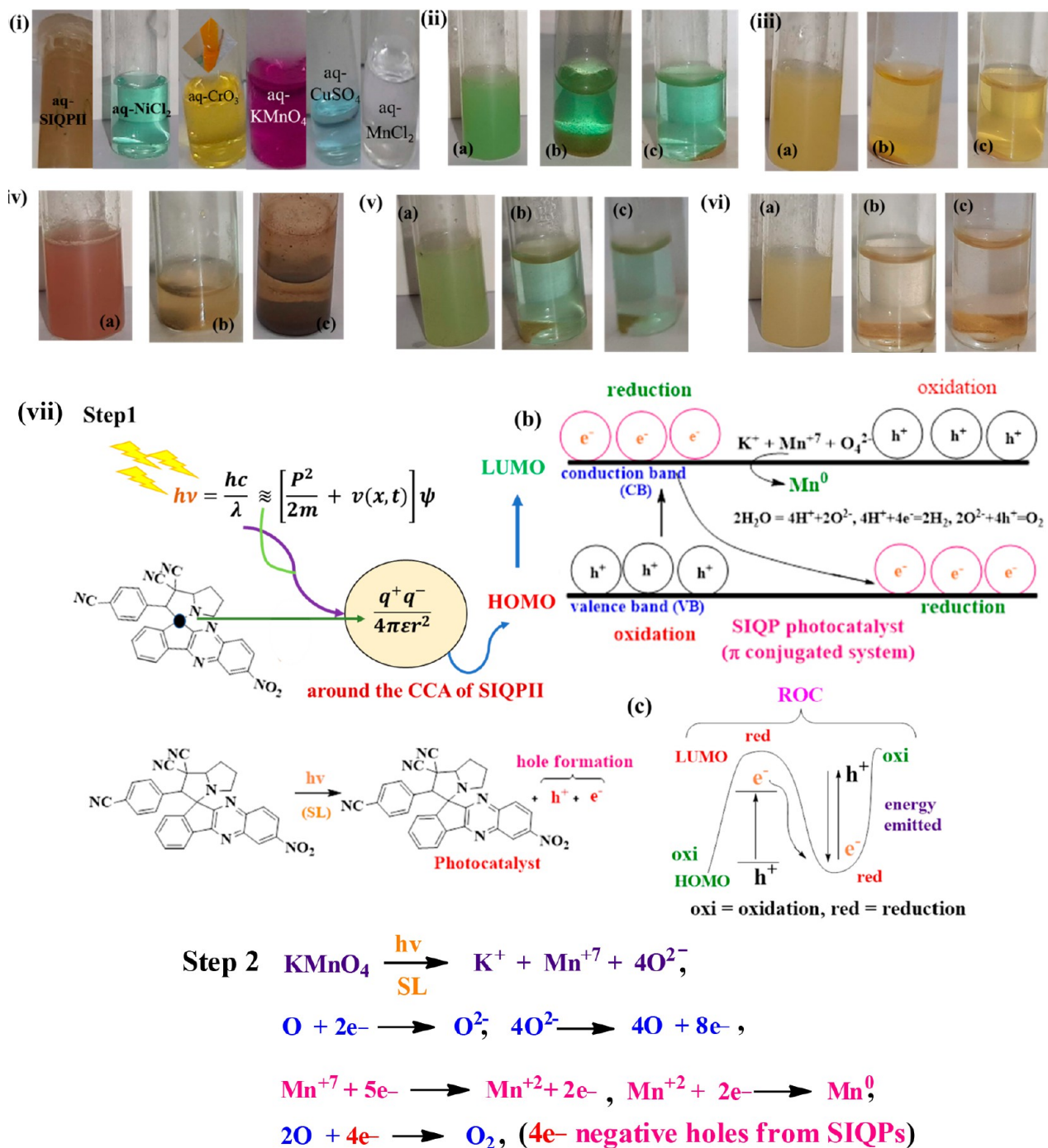


**Figure 16.** (i) Initial color of alone SIQP II in ACN, aq-NiCl<sub>2</sub>, aq-CrO<sub>3</sub>, aq-KMnO<sub>4</sub>, aq-CuSO<sub>4</sub>, and aq-MnCl<sub>2</sub>. Photocatalysis by SIQP II with transition metals (ii) aq-NiCl<sub>2</sub> at (a) *t* = 0, (b) *t* = 36 h, (c) *t* = 38 h, (iii) aq-CrO<sub>3</sub> at (a) *t* = 0 min, (b) *t* = 60 min, (c) *t* = 200 min, (iv) aq-KMnO<sub>4</sub> at (a) *t* = 0, (b) *t* = 26 min, (c) *t* = 30 min, (v) aq-CuSO<sub>4</sub> at (a) *t* = 0, (b) *t* = 16 h, (c) *t* = 18 h, and (vi) aq-MnCl<sub>2</sub> at (a) *t* = 0 min, (b) *t* = 45 min, (c) *t* = 69 min, (vii) mechanism of SIQP II to PCR KMnO<sub>4</sub>.

bottom. The Mn<sup>2+</sup> needs a higher *E*<sub>a</sub> for reduction due to 3d<sup>5</sup>, and the SIQP II reduced Cl<sup>-</sup>: 2Cl<sup>-</sup> + h<sup>+</sup> → Cl<sub>2</sub>. Its e<sup>-</sup> split H<sub>2</sub>O as 2H<sub>2</sub>O + 2HO<sup>-</sup> → 3H<sub>2</sub> + 2O<sub>2</sub> with NiCl<sub>2</sub> (349.22 J/mol) and its least *E*<sub>a</sub> compared to CuSO<sub>4</sub> (419.37 J/mol) due to its (Ni<sup>2+</sup>) large cationic size (Figure 17). Also, the number of unpaired electrons (x = 2, 3d<sup>8</sup>) with NiCl<sub>2</sub> developed a high magnetic dipole moment to reduce a *E*<sub>a</sub> unlike a single unpaired electron (*N* = 1, 3d<sup>9</sup>) with CuSO<sub>4</sub>. Thus, the transition metal formed MOF with SIQPs under SL, whereas dyes like QHIn, MB, and MO reduced by SIQPs with electrolyte produced sodium 2-((4-

hydroxyphenyl)(4-oxidophenyl)methyl)benzoate, Leuco MB, and sodium sulfanilate with *N*<sup>1</sup>,*N*<sup>1</sup>-dimethylbenzene-1,4-diamine, respectively (Scheme 1). The resultant products can be separated using column chromatography and determined with FT-IR, NMR, LC-MS, UV-vis, TGA, and XRD. The QHIn to HIn is based on a medium pH but with electrolytes in the presence of SIQPs at constant pH it was obtained as a colorless sodium 2-((4-hydroxyphenyl)(4-oxidophenyl)methyl)benzoate. It regained a pink color on addition of aq-ethanol HIn and confirmed the QHIn structure. The blue color of MB

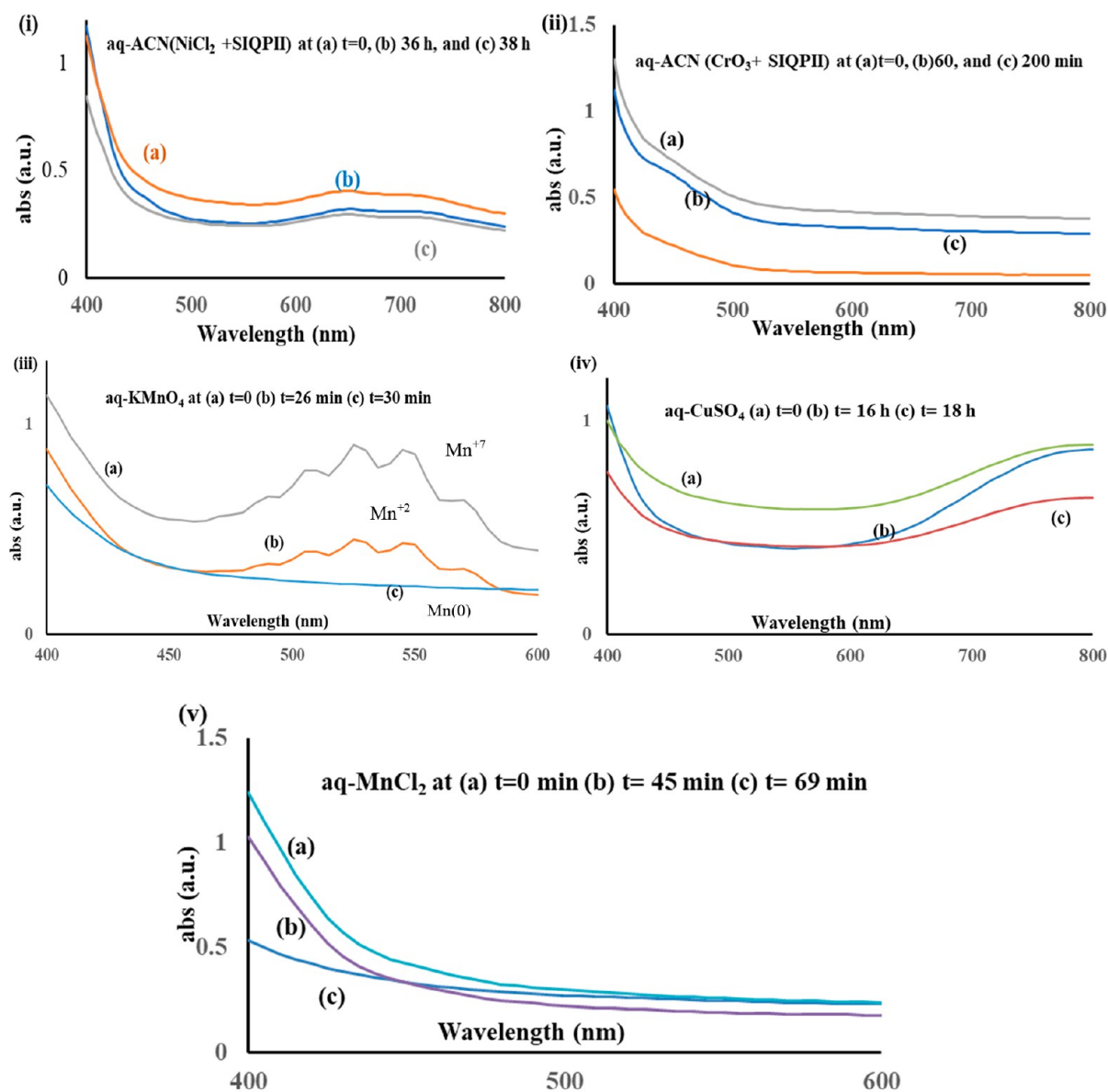


**Figure 17.** UV–vis abs spectra before and after PCR of transition metals by SIQP II.

having quaternary N reduced to colorless Leuco MB on PCR. The SIQPs structure was not degraded; it was confirmed with high end structure determining techniques. The MO with SIQPs alone and in the presence of electrolytes effectively reduced to sodium sulfanilate and  $N^1,N^1$ -dimethylbenzene-1,4-diamine. The SIQPs were not degraded as shown with UV–vis spectroscopy. The recyclable activities of SIQPs photodegraded the persistent pollutant/dyes in four reusable steps. The SIQPs could be readily recovered from a photocatalytic system via centrifuge for reuse for reducing fluorescence dyes in water under UV light irradiation. The SIQP II exhibited  $\sim 47\%$  photocatalytic reduction efficiency of dyes in four successive cycles under SL. The recycled samples have exhibited photocatalytic efficiency in four successive cycles to reduce QHIn by SIQP II at pH 8 is 90, 67, 54, and 47% with NaCl and 82, 70, 51, and 34% with KCl in four successive cycles similar to that of the 100% of freshly prepared SIQP II with NaCl. It has retained an original structure of SIQP II during a photoreduction of QHIn. The SIQP II with MNPs has reduced 28% QHIn in its first cycle compared to freshly used SIQP II with MNPs in the

presence NaCl. This is due to a variable oxidation potential of MNPs. Thus, the SIQPs have excellent photocatalytic activities with a higher stability for reducing the fluorescence dyes at variable pH range.

**2.6. Differential Thermal analysis (DTA).** DTA with a heat holding capacity of SIQPs induces a wt loss (Figure S10(a–c)) where sharper peaks infer thermal energy (TE) of crystalline pyz, phenyl, and NIQ as

$$E = kK_T, E = eV \text{ or } E = \frac{hc}{\lambda} \text{ or } E = h\nu \text{ or } kK_T = h\nu \text{ for } \nu = \frac{kK_T}{h} \quad (14)$$

where  $E$  = energy,  $k$  = Boltzmann distribution constant,  $K_T$  = Kelvin  $T$  constant,  $h$  = Planck constant,  $e$  = oscillating electron,  $V$  = electric potential, and  $\nu$  = frequency. The  $\nu$  of differential wt loss depicted sharper peaks at  $K_T$  calculated with eq 14 (Figure 18 and Table 7). The wt loss elucidates a preferential thermal stability of each constituent. The water released during SIQP synthesis might have developed an azeotrope with SIQP cavities and separated at  $>110^\circ\text{C}$  (Figure S10). The azeotrope



Scheme 1. (a) QHIn, (b) MB, and (c) MO Reduced by SIQPs with Electrolyte Have Produced Sodium 2-((4-Hydroxyphenyl)(4-oxidophenyl)methyl)benzoate, Leuco MB, and Sodium Sulfanilate with  $N^1,N^1$ -Dimethylbenzene-1,4-diamine, Respectively, under SL

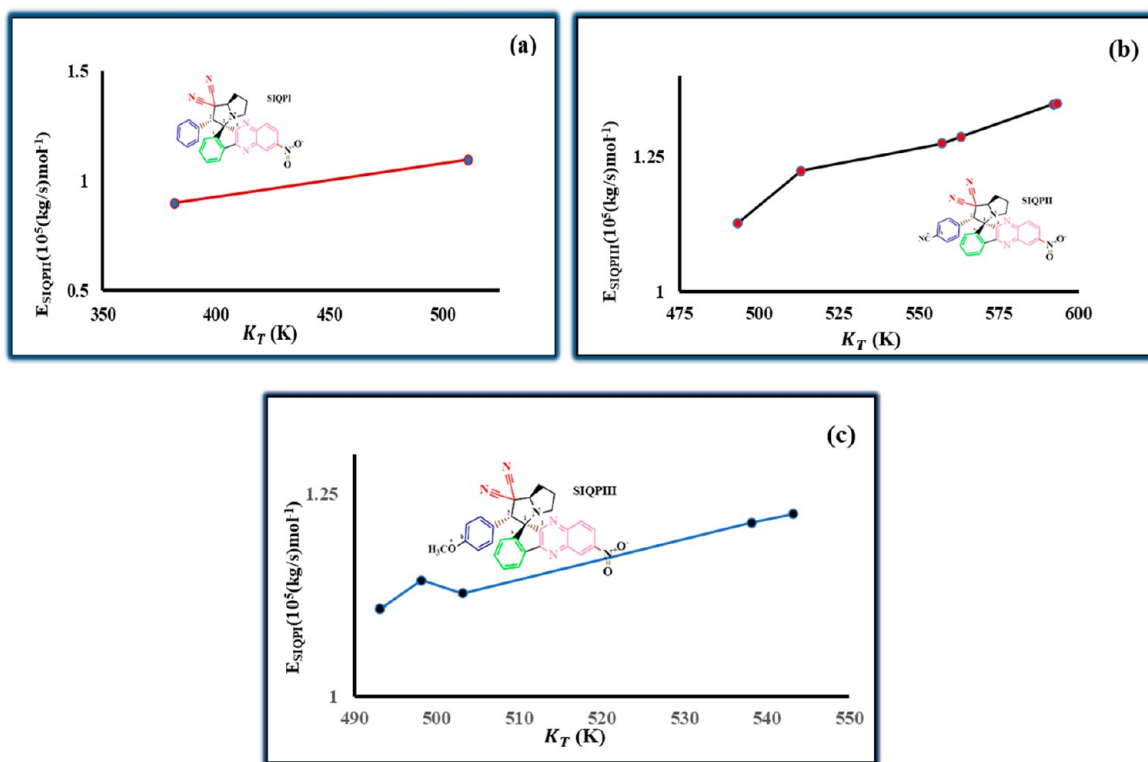
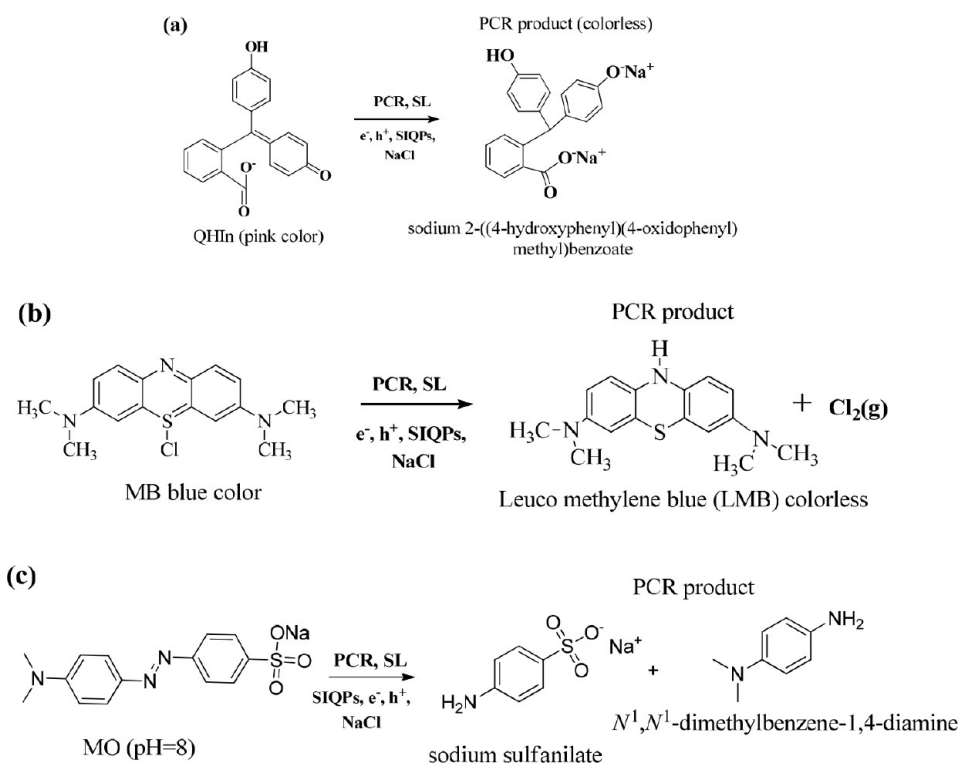


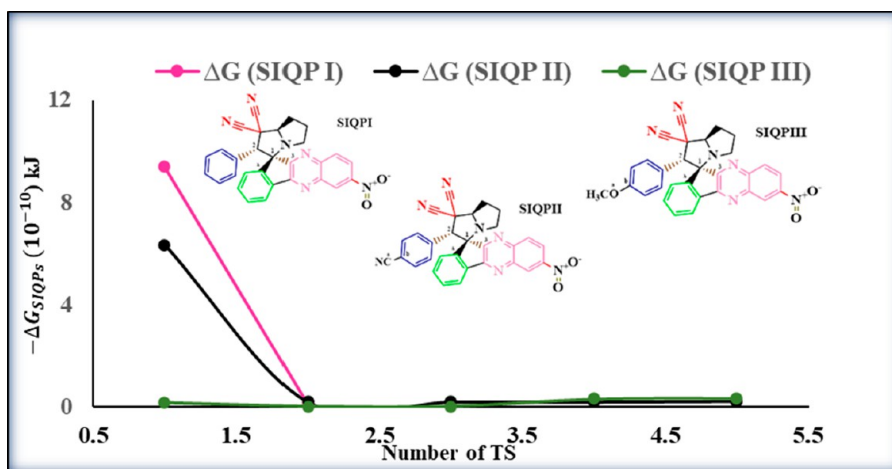
Figure 18.  $E_{\text{SIQPs}}$  (a) I, (b) II, and (c) III with number of TS at  $K_T$ .

attached either with cavities of 2NC or  $\text{NO}_2$  affecting a sharper activity via various electronic motions on raising the  $T$ . The optimized SIQPs are dislocated by twisting the rotation and vibration of bonds where the  $h\nu$  on receiving heat elongates a

bond of FG as per Hook's law.<sup>26</sup> These activities caused a wt loss with  $\Delta H/K_T$ , the  $\Delta H = \Delta q$ , a thermal content at constant pressure. The SIQPI at 108 °C slightly released heat but at 190–290 °C broadened a peak on a heat loss (Figure S10). Initially, a

Table 7.  $\nu$ ,  $E$ ,  $\Delta G$ , and  $E_a$  of TS Generated during Wt Loss at Constant  $K_T$  with Respect to Time

SIQP	TS at Different $K_T$ (K)	$\nu$ ( $10^{13}$ s $^{-1}$ )	$E$ ( $10^{-24}$ kJ)	$\Delta G$ ( $10^{-10}$ kJ)	ESIQPs ( $105(\text{kg}) \text{ J mol}^{-1}$ )
I	1st TS, $K_T = 381.75$	7.9545	5.2706	-9.3891	0.898135
	2nd TS, $K_T = 511.18$	1.0651	7.0573	-0.01212	1.09630
II	1st TS, $K_T = 493.15$	1.0275	6.8082	-6.3362	1.12598
	2nd TS, $K_T = 513.15$	1.0692	7.0845	-0.20647	1.22337
	3rd TS, $K_T = 557.15$	1.1609	7.6919	-0.21228	1.27410
	4th TS, $K_T = 563.15$	1.1734	7.7747	-0.2188	1.28714
	5th TS, $K_T = 592.15$	1.234	8.1751	-0.2454	1.34677
	6th TS, $K_T = 593.15$	1.235	8.1884	-0.2485	1.34842
III	1st TS, $K_T = 493.15$	1.0275	6.8082	-0.1852	1.10803
	2nd TS, $K_T = 498.15$	1.0379	6.8771	-0.0290	1.14301
	3rd TS, $K_T = 503.15$	1.0483	6.9460	-0.0294	1.12686
	4th TS, $K_T = 538.15$	1.1212	7.4291	-0.3332	1.21476
	5th TS, $K_T = 543.15$	1.1317	7.4987	-0.3641	1.22559

Figure 19.  $\Delta G_{\text{SIQPs}}$  with number of TS.

lesser number of molecules and atoms received heat with a sharper wt loss at 230 °C @  $\mu\text{g}/\text{min}$ . The heat evolving and dissipating rates become equal as thermograms are sharper on inducing rotational, vibrational ( $\nu_{\text{vib}}$ ), and transitional energies. The ERG and EWG could have hurdled the HOMO to LUMO transitions. The pattern of thermogram could predict a nature of FG bonded with FP calculating its energy with eq 15

$$E_{\text{vib}} = h\nu \left( \nu + \frac{1}{2} \right) \text{ and } \Delta G = -nRT \ln K_T \quad (15)$$

where  $\Delta G$  = Gibbs free energy,<sup>27</sup>  $n$  = number moles in wt loss at  $K_T$ ,  $R$  = constant, and  $\nu$  = frequency of electrons at transition peaks. Increasing  $T$  induces the TS and at  $K_T$  with @ wt loss. The  $\Delta G^{28}$  is calculated with eq 15 using  $K_T$  and  $R$  values, and the  $n$  is calculated in eq 16.

$$n = \frac{\text{wt loss}}{\text{mol wt of SIQPI}} \quad (16)$$

Putting the first wt loss for the first TS of SIQPI at  $K_T = 381.75$  K in eq 16, the  $n$  is calculated as

$$n = \frac{0.308 \times 10^{-6}}{484.16} = 6.37041 \times 10^{-11}$$

$\Delta G_{\text{SIQPI}}$  is calculated by putting  $n = 6.37041 \times 10^{-11}$ ,  $R = 0.008314$  kJ/mol/K,  $T = 298.15$  K, and  $K_T = 381.75$  K in eq 15 as

$$\Delta G_{\text{SIQPI}} = -6.37041 \times 10^{-11} \times 0.008314 \times 298.15 \times 2.303 \times \log(381.75)$$

$$\Delta G_{\text{SIQPI}} = -9.3891 \times 10^{-10}$$

The  $n$  is calculated for the second TS obtained at  $K_T = 511.03$  K for SIQPI as

$$n = \frac{0.3796 \times 10^{-6}}{484.16} = 7.841222 \times 10^{-10}$$

Putting  $K_T = 511.03$  K along with usual values gives

$$\Delta G_{\text{SIQPI}} = -7.841222 \times 10^{-10} \times 0.008314 \times 298.15 \times 2.303 \times \log(511.03)$$

$$\Delta G_{\text{SIQPI}} = -0.01212 \times 10^{-10}$$

Both the  $\Delta G$  and  $n$  values for each TS are calculated for bond breaking at a specific wt loss (Figure 19 and Table 7). The  $\pi$  conjugation of FP and NIQ of SIQPI has extended delocalization caused by  $\text{NO}_2$  as a major exothermic curve at 220 °C. The CCA may not permit FP delocalization, but due to a similar phase of the  $\pi$  conjugations, the  $\psi$  might still have overcome QEB at 220 °C. On continuous heating, the SIQPs acquire energy  $\Delta E_a$  for a wt loss.  $\Delta E_a$  along with  $\Delta G$  is calculated by fitting wt loss vs  $T$  in Arrhenius<sup>29</sup> eq 17.

$$\frac{n}{n_0} = Ae^{-E_a/RT} \text{ or } \ln(n) = \ln A - \frac{E_a}{R} \frac{1}{T}, \quad \Delta H = E_a - 2RT \quad (17)$$

The C atom of pyz with 2NC has a single covalent bond so no electron cloud was affected. The multiple activities of SIQPII influence the  $\psi$  with specific  $\Delta C_p$  @ 22  $\mu\text{g}/\text{min}$  wt loss at 250 °C. The  $\mu\text{g}/\text{min}$ , a @ wt loss vs  $T$ , is lower as heat generates the internal TS with  $S_1$  to engage the SIQPs rather than a wt loss (Figure S10). The exothermic heat with ERG/OCH<sub>3</sub> has caused a sharper curve as OCH<sub>3</sub> develops its own motions rather shifting its electron cloud toward delocalization. The OCH<sub>3</sub> as a single domain generates its own  $\psi$  despite an oscillation of 2NC at 230 °C. The OCH<sub>3</sub> aligns delocalizing activities to a sharper exothermic curve jointly at 230 °C along with its own oscillations (Figure S10). The exothermic curve at 270 °C infers an optimized OCH<sub>3</sub> oscillation and delocalization together with 2NC and NO<sub>2</sub> FG. The NO<sub>2</sub>, 2NC, and phenyl affect @wt loss on raising a  $T$ , whereas delocalized FP bonded with pyz acted as a free unit. The CCA may selectively allow the robust  $\psi$  affecting delocalization of NIQ. Thus, a CCA with QEB may filter the weak  $\psi$  of respective units; e.g., had CN been absent then a major exothermic curve could have been repeated as SIQPI does not have CN with FP (Figure S10). The extra exothermic curves with SIQPII as CN need energy for oscillations so on further heating the II has weakened the binding forces. SIQPI is a stronger heat dissipator than II and III and may be used in IC/electronic systems for heat dissipation. The CN generates a first exothermic curve at 230 °C and second at 320 °C (Figure S10(b)). The CN triple bond was quenched and restricted oscillatory motions of phenyl at 300 °C. The two closely placed splits infer domains of 2NC and CN at a closure distance to project their impact together; still, a smaller impact of individual CN is depicted with small two peaks (Figure S10(b)). Had the 2NC been together, it could have produced a major impact but these 2NC are not connected to delocalize a phenyl preventing the oscillations. The CN has sharpened the phenyl activity by dissipating the heat that further split the peaks. SIQPII with CN and the III with OCH<sub>3</sub> have caused the additional split which are missing with FP of I except a single curve. The CN of SIQPII split its overall electronic activities as the  $S_1$  or tertiary transitions ( $T_1$ ) in photoluminescence minimize a wt loss at a lower @. Initially, the SIQPII due to an interrupted delocalization with CN generated multiple small curves at low  $T$ . The small curves disappear with rising  $T$  within a short time. The NO<sub>2</sub> and 2NC both have sharply split into curves whereas the phenyl with EWG/CN and ERG have disarrayed. The small splitting is produced by heat-sensitive SIQPII and III from 400 to 450 °C as a heat sensor. The heat generation and dissipation are of the same orders with closely placed transitions. SIQPI with a single  $\Delta G_{\text{SIQPI}}$  at 110 °C, on further heating, stabilizes the molecular motions at 230 °C. SIQPI at 230 °C has produced a single major peak unlike multiple peaks with II and III due to a stabilized  $T$  response. The SIQPII and III distinguish the CN and OMe as the CN generated two TS (Figure S10(b,c)). The NC-phenyl and 2NC-pyz of the SIQPII slightly caused the same influence mutually as the CN stabilized domain does not affect its Lennard-Jones potential. Interacting activities of three sharpened peaks of CN with SIQPII have strongly developed the Born–Oppenheimer approximation<sup>30,31</sup> compared to III as the N atom of CN with sp hybridization mildly influences a delocalized phenyl via a delocalized electron cloud (DLEC) that infers a  $T$ -sensitive

broader peak (Figure S10(b)). The 2NC had generated a broader peak at 325 °C in alignment with the NC-phenyl to influence the DLEC and activities of 2NC. The OCH<sub>3</sub> with hydrophobicity minimized a split between the peaks due to EER of O atom with DLEC with the maximum collisions in SIQPIII (Figure S10(c)). Also, an increase in @wt loss from 21  $\mu\text{g}/\text{min}$  with EWG and 62  $\mu\text{g}/\text{min}$  with ERG infer the II as a stronger photocatalysing sensor (Figure S10). The  $\Delta G_{\text{SIQPs}}$  values are calculated from the wt loss to infer spontaneous photocatalysing activities. The  $\psi_{\text{CN}}$ ,  $\psi_{2\text{CN}}$ ,  $\psi_{\text{pyz}}$ , and  $\psi_{\text{NIQ}}$  of SIQPII have reduced a QEB where the  $e^-$  and  $h^+$  holes photocatalyze<sup>31</sup> dyes. The closely placed sharper splits infer the electronic oscillations of the 1a C atom of pyz bonded with 2NC and another C atom of 2NC. The oscillations of 1a C atom of pyz differ from the 2 and b C atoms of phenyl along with a C atom of CN. A major broader third peak with a lower wt loss infers an equilibrated SIQPII structure as on raising a  $T$ . SIQPII with EWG reorients at 320 °C compared to I and III at 240 and 270 °C, respectively (Figure S10). The delocalized electrons and ERG both move along the pyz and NIQ causing EER with KE ( $p^2/2m$ ) unlike EWG developing PE ( $q^+ q^-/4\pi\epsilon r^2$ ) which aligns the holes of SIQPII compared to ( $p^2/2m$ ) that weaken hole alignments of I and III.

**2.7. Differential Scanning Calorimetry (DSC) Analysis.** NIQ with > CO and NO<sub>2</sub> on heating split at ~207 and ~253.8 °C utilizing -0.0161 and 3.1180 J/g  $\Delta H$ , respectively for their its electronic reorientation (Figure S11(a)). A major break up at ~308.4 °C with 98.33 J/g  $\Delta H$  infers a disruption of van der Waals within NIQ due to DLEC and N atom with extended delocalization. The sharper peaks infer manifolds delocalizing rings and EWG NO<sub>2</sub> (Figure S11(a)). The sharper peaks of SIQPI<sup>32</sup> from 31 to 38.2 °C and 38–72 °C infer a sharper lattice reorientation (Figure S11(b)). The SIQPI is reoriented, so no unused heat is generated, but from 83 to 100 °C the 23.43 mW energy is released. The robust reorientations might have oscillated to partially increase the heat as ROC infers HOMO  $\rightleftharpoons$  LUMO. The HOMO  $\rightarrow$  LUMO  $\rightleftharpoons$  LUMO  $\rightarrow$  HOMO cycles develop a sharper HOMO  $\rightarrow$  LUMO cycle with SIQPI (Figure S11(b)). Initially, HOMO  $\rightarrow$  LUMO activities are stronger from 120–225 °C where HOMO  $\rightarrow$  LUMO equilibrates with equal LUMO  $\rightarrow$  HOMO cycles. SIQPs abruptly collide with KE =  $kT$  expressed as in eq 18.

$$KE = \frac{1}{2}mv^2, \text{ or } kT = \frac{1}{2}mv^2, T = \frac{mv^2}{2k}, \text{ or } T \propto m, \text{ or } T \propto v^2 \quad (18)$$

A prominent DSC exothermic peak is minimized as EWG with SIQPII sharply has reoriented the DLEC (Figure S11(c)). A straight line from 125–200 °C infers no  $T$  effect as the CN have disrupted the  $\psi_{h^+}$  and  $\psi_{e^-}$  to intensify the ROC in SIQPII, whereas no ROC generated from 130 to 200 °C except a mild split at 120 °C on increasing  $T$  and electronic ( $\psi_n \rightarrow \psi_{n^*}$ ,  $\psi_\pi \rightarrow \psi_{\pi^*}$ , and  $\psi_\sigma \rightarrow \psi_{\sigma^*}$ ) transitions of NC-phenyl to minimizing QEB via CCA of SIQPII. The  $\psi$  of FP with  $\psi_\pi \rightarrow \psi_{\pi^*}$  and  $\psi_\sigma \rightarrow \psi_{\sigma^*}$  mutually counterbalanced the energy without increasing the  $T$ . On raising the  $T$ , the  $\psi$  population are counterbalanced in the same ratio, so no extra energy is attained up to 210 °C (Figure S11(c)). A continuous electronic transition of the respective domains generates  $\psi$  that may phase out due to EER utilizing their energy sharply. These activities generate a downward peak at 278 °C as the CCA could induce excessive rotations and vibrations of pyz and NIQ on acquiring energy. The broader peak from 225 to 320 °C infers  $\psi_{\text{pyz}} \neq \psi_{\text{NIQ}}$  templates as their energies largely differ. With SIQPIII, an ineffective broader peak



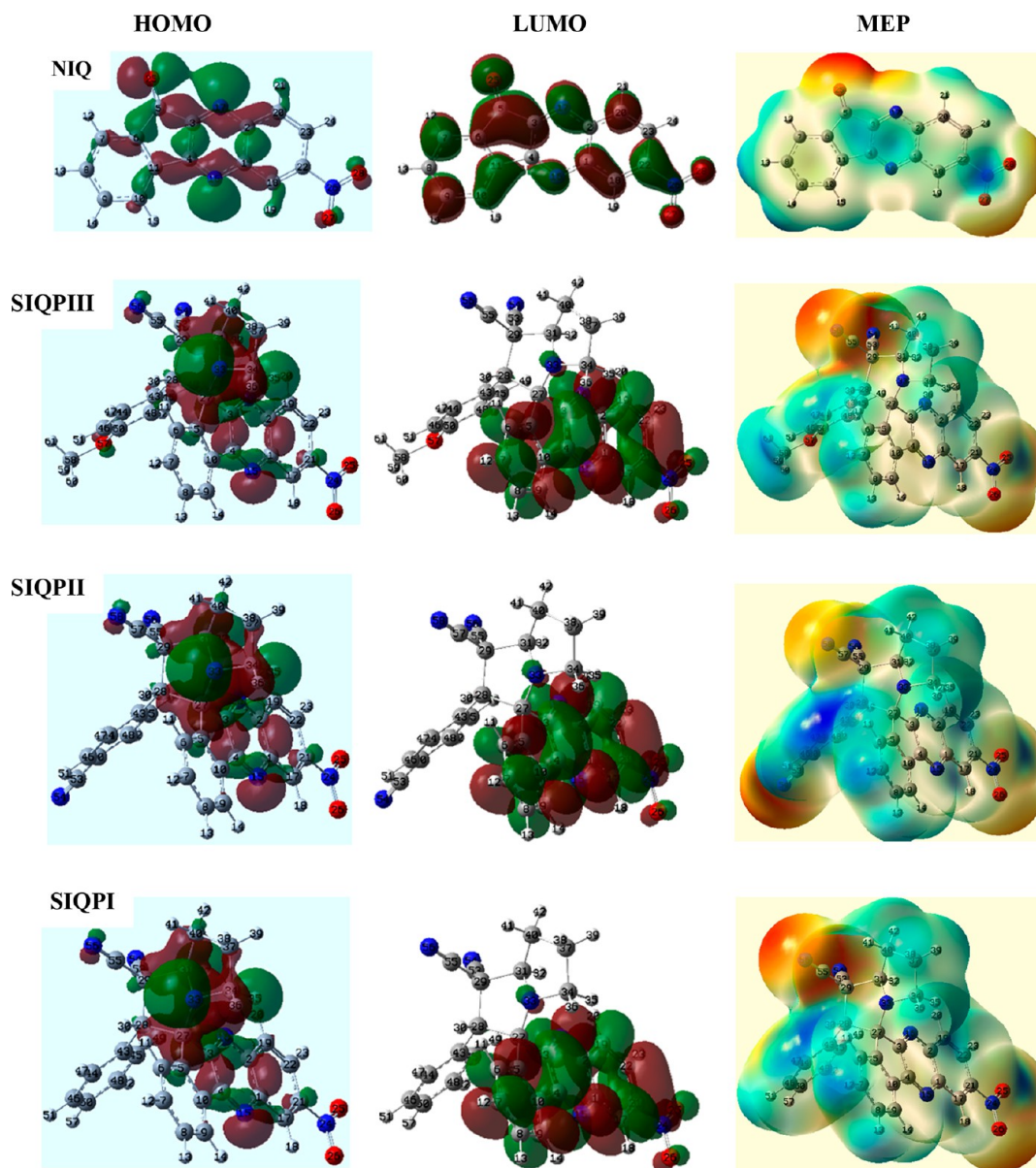


**Figure 20.** HOMO and LUMO (isoval:0.02) and MEP (isoval:0.0004) for NIQ and SIQPs at the B3LYP/6-311++G (df, pd) level.

with a localized milder split is generated at 90–110 °C. The OCH<sub>3</sub> via phenyl resisted –O– electron mildly influence DLEC, and a milder peak at 92 °C is generated. The OCH<sub>3</sub> contrary to CN generates electronic transitions at 278 °C. From 190 to 275 °C, a decrease in heat flow occurs slowly compared to EWG, i.e., CN (Figure S11(c,d)).

**2.8. Density Functional theory (DFT) for Analyzing Electronic Potential of SIQPs.** Quantum mechanical simulation of holes of SIQPs and NIQ have been estimated by fitting G09W at the B3LYP/6-311++G (df, pd) level<sup>33</sup> (Figure S12). Their optimizations were verified in the absence of negative frequency where Koopmans theorem has determined ionization energy ( $I$ ) and electron affinity ( $A$ ) via HOMO and LUMO transitions as  $I = -E_{\text{HOMO}}$  and  $A = -E_{\text{LUMO}}$ . Here electronic chemical potential ( $\chi$ ), global hardness ( $\eta$ ), electrophilicity<sup>34</sup> ( $\omega$ ), and a maximum charge transfer index ( $\Delta N_{\text{max}}$ ) were calculated using DFT<sup>35</sup> with eq 19 as

$$\chi = -\frac{I + A}{2}, \quad \eta = \frac{I - A}{2}, \quad \omega = \frac{\mu^2}{2\eta}, \quad \text{and } \Delta N_{\text{max}} = \frac{I + A}{2(I - A)} \quad (19)$$

GaussView 6.0.16 software was used calculate HOMO and LUMO energies with MEP graphs of SIQPs<sup>36</sup> and NIQ for their active intramolecular interactions (Table S2). The  $\Delta E_{\text{gap}}$  (eV) as SIQPPII (3.5193) > I (3.4586) > III (3.2469) infers the stronger interactions of EWG with dyes in a shorter time. The  $\mu$  and  $\eta$  values (eV) as SIQPPII (–5.2928) < I (–5.1027) < III (–4.9522) and SIQPPII (1.7596) > I (1.7293) > III (1.6234), respectively, infer the II with NC-phenyl as a robust photocatalyst. The  $\omega$  and dipole moment values infer higher electrophilicity index and dipole moment of SIQPPII. The polarizability index ( $\rho$  a.u.) as III (412.3949) > II (411.3741) > I (391.2703) of SIQPPII and III with CN and OCH<sub>3</sub>, respectively, is higher than that of I. Electron density and surface analysis were simulated with the molecular orbital to infer an interactive region higher with SIQPPII (Figure 20). The HOMO density with NIQ is localized on a central five-membered ring and partially on the O atoms of

substituted NO<sub>2</sub> while the LUMO exists on surfaces. Molecular electrostatic potential expressed by dark red color infers an active site of SIQPs for their electrophilic and nucleophilic activities, respectively. The CN<sup>37</sup> is favored over O atoms of NO<sub>2</sub> in electrophilic attacks as a major hydrophilic surface area. Pyz due to a neutral electrostatic potential has no role in electrophilic and nucleophilic attacks (Figure 20), whereas with NIQ, the O atom of >C=O is more reactive than the other O atoms of NO<sub>2</sub> for electrophilic sites. Reactive behavior and sites of SIQPs and NIQ are evaluated by DFT<sup>38</sup> at the B3LYP/6-311++G (df, pd) level.

### 3. CONCLUSION

A complete photocatalysis of dyes with SIQP photocatalysts is achieved in mixed solvent under SL. SIQPI, II, and III with NaCl reduced the QHIn in 120, 28, and 50 min compared to 138, 58, and 63 with KCl, respectively, contrary to MNPs in 2880 min with SIQPII. The  $\Phi$  of QHIn for PCR by SIQPs are reported first time. SIQPII having EWG and III having ERG with strong electrolytes have acted as a robust photocatalyst to PCR dyes. The electrolytes with SIQPs have dissolved a biphasic aq-EtOH +QHIn+NaOH and aq-ACN+SIQPs solutions to minimize QEB via PCI. The electrolytes had mildly activated the SIQPII with MNPs to reduce QHIn in 2880 min unlike 28 and 58 min for SIQPII with NaCl and KCl, respectively, and the MNPs alone could not PCR the QHIn. The CCA has partitioned the electronic clouds of the pyz and NIQ templates of SIQPII causing a weak PCI with MNPs except to create energy at surfaces. The photoreduction of a persistent pollutant dye like QHIn at pH 8 with electrolytes and the BBR, MO (with T effect), and CuSO<sub>4</sub>, MnCl<sub>2</sub>, CrO<sub>3</sub>, and NiCl<sub>2</sub> transition-metal ions with electrolytes at pH 4 and 8 are studied with SIQPs. The photoreduction of Mn<sup>7+</sup> to Mn<sup>0</sup> with SIQPII under SL developed NPs of Mn via a greener method, whereas other transition-metal ions have formed MOF. Alternatively, the Mn NPs could have been developed the MOF. The dye photo-reduction depends on pH, T, and nature of electrolyte. The PCR activities of SIQPs are being pursued to focus their scope for structural change of biomolecules of the biological systems. This approach could be applied for photocatalysis, electrocatalysis, and thermocatalysis or in combination. Eventually, the photo-mechanism could pave a way for a sustainable photodegradation of waste biomass.

### 4. EXPERIMENTAL SECTION

**4.1. Materials.** The chemical reagents were procured from Sigma-Aldrich. Thin-layer chromatography (TLC) plate, analytical grade hexane (Sigma-Aldrich  $\geq 99\%$ ), ethyl acetate (Sigma-Aldrich  $\geq 99\%$ ), dichloromethane (DCM) (Sigma-Aldrich  $\geq 99.8\%$ ), dimethylformamide (DMF) (Sigma-Aldrich  $\geq 99.8\%$ ), acetone (Sigma-Aldrich  $\geq 99.9\%$ ), MeOH (Sigma-Aldrich  $\geq 99.9\%$ ), ACN (Sigma-Aldrich  $\geq 99.8\%$ ), and solvents were redistilled. Benzaldehyde, *p*-cyanobenzaldehyde, *p*-methoxybenzaldehyde, ninhydrin, malononitrile, lithium bromide, sodium hydroxide, HIn, barium chloride, acetic acid, L-proline, magnetic beads, EtOH, GO, NaCl, KCl, and Whatman filter paper were used as received; the details are reported.

**4.2. Characterization Methods.** SIQPs<sup>1</sup> were characterized by <sup>1</sup>H and <sup>13</sup>C NMR (500 MHz, Bruker Avance Spectrometer) in CDCl<sub>3</sub> using TMS as an internal standard, FT-IR spectra from 200 to 800 cm<sup>-1</sup> with KBr pellets on PerkinElmer TL8000 TG-IR interface, DLS (NPA152-31A-

0000-000-90M, Metrohm), DTA/DTG (SII TG/DTA 7300, EXSTAR), XRD (Philips X'pert MPD System), AFM (Multi-mode Scanning Probe Microscope, Bruker), and PCR study via UV-vis (190–1100 nm with UV-1800 SHIMADZU (UV Spectrophotometer) in ESI mode) and fluorescent spectroscopy (FluoroMax-4 Spectrofluorometer HORIBA) with computational study.

**4.3. Synthesis of SIQPs.** A condensation reaction of ninhydrin, 4-nitro-1,2-phenylenediamine in acetic acid, and methanol synthesized a linear NIQ (Scheme S1) at NTP. The NIQ mixed with derivatives of benzylidene malononitrile separately with L-proline in methanol synthesized SIQPs at ~110 °C. For SIQPI, the 2-benzylidenemalononitrile (1.0 mmol, 1.0 equiv, 154.5 g) (Scheme S2), SIQPII, 2-(4-cyanobenzylidene)malononitrile (1.0 mmol, 1.0 equiv, 131.1 g) (Scheme S3), and SIQPIII, 2-(4-methoxybenzylidene) (Scheme S4) were separately added to NIQ (1.0 mmol, 1.0 equiv, 277 g) and L-proline (1.0 mmol, 1.0 equiv, 126.5 g) with methanol (15 mL) on stirring and refluxing for 3 h. The SIQPs were structurally characterized with <sup>1</sup>H and <sup>13</sup>C NMR and FT-IR to widen their PCR applications (Schemes S5–S7).

**4.4. Synthesis of GO and MNPs (Fe<sub>3</sub>O<sub>4</sub>).** Graphite flakes (1.5 g) and KMnO<sub>4</sub> (9g) were taken in a 500 mL RB flask to synthesizing GO. A 5.8:1 ratio of H<sub>2</sub>SO<sub>4</sub> and H<sub>3</sub>PO<sub>4</sub> was transferred to a RB flask with continuous stirring at 293.15 K. A dark grayish suspension produced at NTP was refluxed at 328.15 K @800 rpm for 12 h. To avoid a viscousness with time, ice-cold water was slowly appended to the mixture that raised T, 363.15 K, to form a dark brown suspension. The unused KMnO<sub>4</sub> and MnO<sub>2</sub> were reduced to colorless MnSO<sub>4</sub> with a simultaneous oxidation of graphene with a nascent oxygen produced *in situ*. Later, 30% H<sub>2</sub>O<sub>2</sub> addition had developed a brown dark yellowish suspension that was centrifuged and washed with 5% HCl to remove the metallic impurities. Final washing with chilled water has removed water-soluble impurities at neutral pH. The GO residue was coagulated in 45 mL of petroleum ether and dried for 43 h at 323 K in oven. A dark brownish mass of GO was obtained and exfoliated in water with 1 mg/mL for 1 h to obtain pure GO at NTP by sonication @30 kHz characterized by UV-vis. The MNPs were synthesized by coprecipitation of Fe<sup>3+</sup> and Fe<sup>2+</sup> out of FeCl<sub>3</sub> and FeSO<sub>4</sub>·7H<sub>2</sub>O salts in 2:1 ratio with aq 8 M NaOH on heating at 363.15 K for 2 h to yield 95% MNPs and were used for fluorescence to PCR with SIQPII.

### ■ ASSOCIATED CONTENT

#### SI Supporting Information

The Supporting Information is available free of charge at <https://pubs.acs.org/doi/10.1021/acsomega.2c05103>.

<sup>1</sup>H NMR, <sup>13</sup>C NMR, XRD, AFM, DSC, DLS, FT-IR, and UV-vis spectral data, fluorescence spectroscopy, and DFT (PDF)

### ■ AUTHOR INFORMATION

#### Corresponding Author

Man Singh – School of Chemical Sciences, Central University of Gujarat, Gandhinagar 382030, India; [orcid.org/0000-0002-0706-3763](https://orcid.org/0000-0002-0706-3763); Phone: +91-079-23260210; Email: [mansingh50@hotmail.com](mailto:mansingh50@hotmail.com); Fax: +91-079-23260076



## Author

Renu Kumari – School of Chemical Sciences, Central University of Gujarat, Gandhinagar 382030, India

Complete contact information is available at:

<https://pubs.acs.org/10.1021/acsomega.2c05103>

## Notes

The authors declare no competing financial interest.

## ACKNOWLEDGMENTS

The authors wish to express sincere appreciation to the following for their considerable assistance in this work: Central University of Gujarat, India, for infrastructural support, CSIR Bhavnagar for XRD spectroscopy, and Gujarat University, India, for Fluorescence spectroscopy. DFT calculations were performed at TUBITAK-ULAKBIM, High Performance and Grid Computing Center (TRUBA resources), Turkey.

## REFERENCES

- (1) Kumari, R.; Singh, M. Photocatalytic Reduction of Fluorescent Dyes in Sunlight by Newly Synthesized Spiroindenoquinoxaline Pyrrolizidines. *ACS Omega* **2020**, *5*, 23201–23218.
- (2) Salama, A.; Mohamed, A.; Aboamera, N. M.; Osman, T. A.; Khattab, A. Photocatalytic degradation of organic dyes using composite nanofibers under UV irradiation. *Appl. Nanosci.* **2018**, *8*, 155–161.
- (3) Dev, S.; Singh, M. Metallic sulfide nanoparticles anchored graphene oxide: Synthesis, characterization and reduction of methylene blue to leuco methylene blue in aqueous mixtures. *J. Phys. Chem. Solids* **2020**, *139*, 109335.
- (4) Liu, J.; Lu, Y. FRET Study of a Trifluorophore-Labeled DNAzyme. *J. Am. Chem. Soc.* **2002**, *124*, 15208–15216.
- (5) Tan, L.-L.; Ong, W.-J.; Chai, S.-P.; Mohamed, A. R. Reduced graphene oxide-TiO<sub>2</sub> nanocomposite as a promising visible-light-active photocatalyst for the conversion of carbon dioxide. *Nanoscale Research Letters* **2013**, *8*, 465.
- (6) Bratovčić, A. Photocatalytic degradation of organic compounds in waste waters. *Technologica Acta* **2019**, DOI: 10.5281/zenodo.2563022.
- (7) Buev, E. M.; Moshkin, V. S.; Sosnovskikh, V. Y. Reactivity of spiroanthraceneoxazolines with cyclopropanes: An approach to the oxindole alkaloid scaffold. *Tetrahedron Letters* **2018**, *59* (37), 3409–3412.
- (8) Pandya, S. R.; Singh, M. Dispersion and optical activities of newly synthesized magnetic nanoparticles with organic acids and dendrimers in DMSO studied with UV/vis spectrophotometry. *J. Mol. Liq.* **2015**, *211*, 146–156.
- (9) Kiseleva, A.; Kiselev, G.; Kessler, V.; Seisenbaeva, G.; Gets, D.; Rumyantseva, V.; Lyalina, T.; Fakhardo, A.; Krivoschapkin, P.; Krivoschapkina, E. Optically Active Hybrid Materials Based on Natural Spider Silk. *ACS Appl. Mater. Interfaces* **2019**, *11*, 22962–22972.
- (10) Mantry, L.; Maayuri, R.; Kumar, V.; Gandeepan, P. Photoredox catalysis in nickel-catalyzed C-H functionalization. *Beilstein J. Org. Chem.* **2021**, *17*, 2209–2259.
- (11) Shahrestani, N.; Salahi, F.; Tavakoli, N.; Jadidi, K.; Hamzehloueian, M.; Notash, B. Asymmetric Synthesis Approach of Enantiomerically Pure Spiro-Indenoquinoxaline Pyrrolidines and Spiro-Indenoquinoxaline Pyrrolizidines. *Tetrahedron Asymmetry* **2015**, *26*, 1117–1129.
- (12) Jangid, A. K.; Malik, P.; Singh, M. Mineral acid monitored physicochemical studies of oil in water nanoemulsions. *J. Mol. Liq.* **2018**, *259*, 439–452.
- (13) Malik, P.; Inwati, G. K.; Mukherjee, T. K.; Singh, S.; Singh, M. Green silver nanoparticle and Tween-20 modulated pro-oxidant to antioxidant curcumin transformation in aqueous CTAB stabilized peanut oil emulsions. *J. Mol. Liq.* **2019**, *291*, 111252.
- (14) Naikwade, G. A.; Jagdale, B. M.; Kale, P. D.; Gophane, D. A.; Garadkar, M. K.; Rashinkar, S. G. Photocatalytic Degradation of Methyl Orange by Magnetically Retrievable Supported Ionic Liquid Phase Photocatalyst. *ACS Omega* **2020**, *5*, 131–144.
- (15) Huang, X.; Wang, R.; Tifeng, Jiao; Zou, G.; Zhan, F.; Yin, J.; Zhang, L.; Zhou, J.; Peng, Q. Facile Preparation of Hierarchical AgNP-Loaded MXene/Fe<sub>3</sub>O<sub>4</sub>/Polymer Nanocomposites by Electrospinning with Enhanced Catalytic Performance for Wastewater Treatment. *ACS Omega* **2019**, *4*, 1897–1906.
- (16) Bandaria, N. J.; Cheatum, M. C.; Kohlen, A. Examination of Enzymatic H-Tunneling through Kinetics and Dynamics. *J. Am. Chem. Soc.* **2009**, *131*, 10151–10155.
- (17) Hummer, G.; Pratt, L. R.; Garcia, A. E. Free Energy of Ionic Hydration. *J. Phys. Chem.* **1996**, *100*, 1206–1215.
- (18) Mazzanti, S.; Manfredi, G.; Barker, J. A.; Antonietti, M.; Savateev, A.; Giusto, P. Carbon Nitride Thin Films as All-In-One Technology for Photocatalysis. *ACS Catal.* **2021**, *11*, 11109–11116.
- (19) Weber, F.; Sagstuen, E.; Zhong, Q.-Z.; Zheng, T.; Tiainen, H. Tannic Acid Radicals in the Presence of Alkali Metal Salts and Their Impact on the Formation of Silicate-Phenolic Networks. *ACS Appl. Mater. Interfaces* **2020**, *12*, 52457–52466.
- (20) Islam, B. Md.; Yanagida, M.; Shirai, Y.; Nabetani, Y. O.; Miyano, K. NiO<sub>x</sub> Hole Transport Layer for Perovskite Solar Cells with Improved Stability and Reproducibility. *ACS Omega* **2017**, *2*, 2291–2299.
- (21) Wang, F.; Li, F. L.; Xu, M. M.; Yu, H.; Zhang, J. G.; Xia, H. T.; Lang, J. P. Facile synthesis of a Ag(I)-doped coordination polymer with enhanced catalytic performance in the photodegradation of azo dyes in water. *J. Mater. Chem. A* **2015**, *3*, 5908.
- (22) Saleh, R.; Djaja, N. F. UV light photocatalytic degradation of organic dyes with Fe-doped ZnO nanoparticles. *Superlattices Microstruct.* **2014**, *74*, 217–233.
- (23) Li, Y.; Liu, Y.; Wang, J.; Uchaker, E.; Zhang, Q.; Sun, S.; Huang, Y.; Li, J.; Cao, G. Titanium alkoxide induced BiOBr-Bi<sub>2</sub>WO<sub>6</sub> mesoporous nanosheet composites with much enhanced photocatalytic activity. *J. Mater. Chem. A* **2013**, *1*, 7949–7956.
- (24) Oana, G.; Gabriela, B.; Mihaela, D. L.; Maria, M. Methanation of CO<sub>2</sub> Using MIL-53-Based Catalysts: Ni/MIL-53-Al<sub>2</sub>O<sub>3</sub> versus Ni/MIL-53. *Catal.* **2021**, *11*, 1412.
- (25) Kashinath, K.; Swaroop, P.; Reddy, D. A green synthetic route to antimalarial and antibacterial agent CJ-15,801 and its isomer cis-CJ-15,801. *RSC Adv.* **2012**, *2*, 3596–3598.
- (26) Bazant, M. Z. Theory of Chemical Kinetics and Charge Transfer based on Nonequilibrium Thermodynamics. *Acc. Chem. Res.* **2013**, *46*, 1144–1160.
- (27) Chashchikhin, V.; Rykova, E.; Bagaturyants, A. Calculations of the Gibbs Free Energy of Adsorption of Some Small Molecules and Amino Acid Decomposition Products on MCM-41 Mesoporous Silica. *J. Phys. Chem. Lett.* **2013**, *4*, 2298–2302.
- (28) Campbell, T. C. The Degree of Rate Control: A Powerful Tool for Catalysis Research. *ACS Catal.* **2017**, *7*, 2770–2779.
- (29) Piskulich, A. Z.; Mesele, O. O.; Thompson, H. W. Activation Energies and Beyond. *J. Phys. Chem. A* **2019**, *123*, 7185–7194.
- (30) Ohno, T.; Tsubota, T.; Miyayama, S.; Sayama, K. Selective oxidation of benzaldehyde derivatives on TiO<sub>2</sub> photocatalysts modified with fluorocarbon group. *Catal. Lett.* **2005**, *102*, 207–210.
- (31) Izmaylov, A. F.; Franco, I. Entanglement in the Born-Oppenheimer Approximation. *J. Chem. Theory Comput.* **2017**, *13*, 20–28.
- (32) Jin, Y.; Govoni, M.; Wolfowicz, G.; Sullivan, S. E.; Heremans, F. J.; Awschalom, D. D.; Galli, G. Photoluminescence spectra of point defects in semiconductors: Validation of first-principles calculations. *Phys. Rev. Mater.* **2021**, *5*, 084603.
- (33) Chengteh, L.; Weitao, Y.; Robert, G. P. Development of the Colle-Salvetti correlation-energy formula into a functional of the electron density. *Phys. Rev.* **1988**, *38*, 785–789.
- (34) Klare, H. F. T.; Oestreich, M. The Power of the Proton: From Superacidic Media to Superelectrophile Catalysis. *J. Am. Chem. Soc.* **2021**, *143*, 15490–15507.
- (35) Koopmans, T. Über die Zuordnung von Wellenfunktionen und Eigenwerten zu den Einzelnen Elektronen Eines Atoms. *Physical.* **1934**, *1*, 104–113.



- (36) Parr, R. G. Density Functional Theory of Atoms and Molecules. *Horizons of Quantum Chemistry* **1980**, *3*, 5–15.
- (37) Sahoo, K. S.; Teixeira, F. I.; Naik, A.; Heske, J.; Cruz, D.; Antonietti, M.; Savateev, A.; Kühne, D. T. Photocatalytic Water Splitting Reaction Catalyzed by Ion-Exchanged Salts of Potassium Poly(heptazine imide) 2D Materials. *J. Phys. Chem. C* **2021**, *125*, 13749–13758.
- (38) Kurfman, A. L.; Odbadrakh, T. T.; Shields, C. G. Calculating Reliable Gibbs Free Energies for Formation of Gas-Phase Clusters that Are Critical for Atmospheric Chemistry:  $(\text{H}_2\text{SO}_4)_3$ . *J. Phys. Chem. A* **2021**, *125*, 3169–3176.